

SUBARU ADAPTIVE-OPTICS HIGH-SPATIAL-RESOLUTION INFRARED K - AND L' -BAND IMAGING SEARCH FOR DEEPLY BURIED DUAL AGNS IN MERGING GALAXIES

MASATOSHI IMANISHI¹ AND YURIKO SAITO¹

Subaru Telescope, 650 North A'ohoku Place, Hilo, Hawaii 96720, U.S.A.

Astrophysical Journal

ABSTRACT

We present the results of infrared K - ($2.2\ \mu\text{m}$) and L' -band ($3.8\ \mu\text{m}$) high-spatial-resolution ($<0''.2$) imaging observations of nearby gas- and dust-rich infrared luminous merging galaxies, assisted by the adaptive optics (AO) system on the Subaru 8.2-m telescope. We investigate the presence and frequency of red $K - L'$ compact sources, which are sensitive indicators of active galactic nuclei (AGNs), including AGNs that are deeply buried in gas and dust. We observed 29 merging systems and confirmed at least one AGN in all but one system. However, luminous dual AGNs were detected in only four of the 29 systems ($\sim 14\%$), despite our method's being sensitive to buried AGNs. For multiple nuclei sources, we compared the estimated AGN luminosities with supermassive black hole (SMBH) masses inferred from large aperture K -band stellar emission photometry in individual nuclei. We found that mass accretion rates onto SMBHs are significantly different among multiple SMBHs, such that larger-mass SMBHs generally show higher mass accretion rates when normalized to SMBH mass. Our results suggest that non-synchronous mass accretion onto SMBHs in gas- and dust-rich infrared luminous merging galaxies hampers the observational detection of kiloparsec-scale multiple active SMBHs. This could explain the significantly smaller detection fraction of kiloparsec-scale dual AGNs when compared with the number expected from simple theoretical predictions. Our results also indicate that mass accretion onto SMBHs is dominated by local conditions, rather than by global galaxy properties, reinforcing the importance of observations to our understanding of how multiple SMBHs are activated and acquire mass in gas- and dust-rich merging galaxies.

Subject headings: galaxies: active — galaxies: nuclei — galaxies: Seyfert — galaxies: starburst — quasars: supermassive black holes — infrared: galaxies

1. INTRODUCTION

Recent observations have revealed that supermassive black holes (SMBHs) are ubiquitously present at the center of galaxy spheroidal components, and that the masses of SMBHs and spheroidal stars are correlated (Magorrian et al. 1998; Ferrarese & Merritt 2000; Gültekin et al. 2009; McConnell & Ma 2013), suggesting that SMBHs are an important galaxy ingredient whose formation is closely related to galaxy formation. The widely accepted cold dark matter-based galaxy formation theories postulate that small gas-rich galaxies merge and grow into massive galaxies, as seen in the present-day universe (White & Rees 1978). If SMBHs are present in the progenitor gas-rich small galaxies, then the merging galaxies should have multiple SMBHs. In this case, kiloparsec-scale dual active galactic nuclei (AGNs) are expected to be common if the mass accretion onto both SMBHs is sufficiently high to create luminous observable AGNs (Colpi & Dotti 2011).

Optical spectroscopic searches for AGNs with double-peaked emission lines (Wang et al. 2009; Liu et al. 2010; Smith et al. 2010; Liu et al. 2011; Pilyugin et al. 2012; Ge et al. 2012; Barrows et al. 2013) and subsequent follow-up observations at other wavelengths have been extensively performed in the search for kiloparsec-scale dual AGNs (Fu et al. 2011; Rosario et al. 2011; Shen et al. 2011; Tingay & Wayth 2011; Comerford et al. 2012; Fu

et al. 2012; Liu et al. 2013). These studies have provided some examples of kiloparsec-scale dual AGNs, but the detected fraction of optically identifiable kiloparsec-scale dual AGNs ($< \text{a few } \%$) is significantly smaller than the number derived from the simple theoretical prediction that the majority of galaxy mergers should have multiple SMBHs and become dual AGNs if both SMBHs are sufficiently mass-accreting (Rosario et al. 2011; Yu et al. 2011). Several scenarios have been proposed to reconcile this discrepancy between theory and observations, but it is still unclear which scenario is most likely. First, double-peaked emission is expected only in dual active SMBHs whose orbital planes are aligned relatively edge-on along our line of sight. Those systems whose orbital planes are aligned face-on are overlooked with these methods (Rosario et al. 2011; Wang et al. 2012). Although this scenario may be able to explain the discrepancy by a factor of a few, it is probably difficult to account for the difference by more than an order of magnitude, provided that the alignment of the orbital planes of two active SMBHs is random in terms of our line-of-sight. A second, more plausible explanation is that most AGNs in gas-rich galaxy mergers are deeply buried in gas and dust along virtually all directions (Hopkins et al. 2005, 2006) and can become optically elusive (Maiolino et al. 2003; Rosario et al. 2011). Third, it is also possible that even though multiple SMBHs are present, only one of them has sufficient mass accretion to be observationally detectable as an AGN (i.e., non-synchronous SMBH mass accretion) during galaxy mergers (van Wassenhove et al. 2012). If we are to unveil observationally the true

Electronic address: masa.imanishi@nao.ac.jp

¹ Department of Astronomy, School of Science, Graduate University for Advanced Studies (SOKENDAI), Mitaka, Tokyo 181-8588

fraction of kiloparsec-scale dual AGNs in gas- and dust-rich merging galaxies, it is of particular importance to apply observational methods that are sensitive to AGNs whose SMBHs orbital motion is relatively face-on along our line-of-sight and to deeply buried AGNs.

High-spatial-resolution imaging observations at the wavelengths of strong dust penetration are a powerful tool for this purpose because imaging observations can, in principle, preferentially detect AGNs with face-on multiple SMBH orbit geometry, and buried AGNs are detectable at such wavelengths. X-rays in the 2–10 keV range have higher dust-penetrating power than the optical in the Galactic interstellar medium (Ryter 1996), and it is well known that an AGN is a much stronger X-ray emitter (relative to the bolometric luminosity) than a starburst (Ranalli et al. 2003; Shang et al. 2011), so X-ray observations are expected to be sensitive to AGNs, including obscured ones. In fact, strong dual AGN candidates were discovered from 2–10 keV X-ray observations of several nearby gas- and dust-rich infrared luminous merging galaxies (Komossa et al. 2003; Ballo et al. 2004; Bianchi et al. 2008; Piconcelli et al. 2010; Koss et al. 2011; Fabbiano et al. 2011). Although the presence of dual AGNs is strongly suggested, the observed 2–10 keV X-ray emission is, in most cases, only a scattered component behind Compton-thick ($N_{\text{H}} > 10^{24} \text{ cm}^{-2}$) obscuring material rather than a directly transmitted component. Thus, the intrinsic AGN X-ray luminosity is difficult to estimate because the scattering efficiency is unknown. To extend the 2–10 keV X-ray dual AGN survey systematically to gas- and dust-rich merging galaxies, the Chandra X-ray Observatory, with its spatial resolution of $\sim 0''.5$, is a particularly powerful tool for spatially resolving closely separated multiple AGNs. In fact, the Chandra X-ray Observatory has been used to find obscured dual AGNs in further gas- and dust-rich merging galaxies (Teng et al. 2005; Iwasawa et al. 2011b; Teng et al. 2012; Koss et al. 2012; Liu et al. 2013). However, the detected X-ray fluxes are, in many cases, so faint that detailed spectral analysis is hampered. Both the scattered X-ray component of Compton-thick obscured AGNs and the emission originating from stars can reproduce the observed faint X-ray fluxes, often making it difficult to interpret the detected X-ray emission as solid evidence for an AGN (Teng et al. 2009; Iwasawa et al. 2011b; Liu et al. 2013). X-ray observations at >10 keV could directly detect transmitted X-ray emission from some mildly Compton-thick AGNs (Itoh et al. 2008), but the spatial resolution at >10 keV is still insufficient ($>15''$) (Harrison et al. 2013) to spatially resolve many interesting closely separated dual AGNs.

High-spatial-resolution radio observation using the VLBI technique is another powerful tool to detect closely separated dual AGNs, as radio wavelengths are less susceptible to dust extinction (Rodriguez et al. 2006). However, the radio VLBI technique is sensitive only to a small fraction of radio-loud AGN population, and it is not sensitive to the radio-quiet AGNs that comprise the majority of the AGN population (Goldschmidt et al. 1999; White et al. 2000). The very small detectable fraction ($<0.05\%$) of dual AGNs discovered using this radio VLBI technique (Burke-Spolaor 2011) is difficult to interpret directly in relation to the actual fraction of dual AGNs.

Infrared observations at $>2 \mu\text{m}$ are potentially another effective (even improved) method for investigating buried

dual AGNs in gas- and dust-rich merging galaxies. First, compared with the optical, dust extinction is substantially reduced ($<0.06 \times A_{\text{V}}$) (Nishiyama et al. 2008, 2009). Additionally, AGNs, including both radio-loud and radio-quiet ones, are observationally distinguishable from starbursts. Strong polycyclic aromatic hydrocarbons (PAH) emission features seen at 3–20 μm are usually observed in starbursts, but not in pure AGNs (Moorwood 1986; Imanishi & Dudley 2000), due to the destruction of PAHs by strong AGN X-ray emission (Voit 1992). In a pure AGN, a PAH-free continuum due to AGN-heated, large ($\sim 0.1 \mu\text{m}$) hot dust grains is observed. Thus, infrared spectroscopy can be a unique means to find obscured AGNs by separating them from starburst activity, as demonstrated by the successful detection of many buried AGNs in the brightest main nuclei of gas- and dust-rich merging galaxies (Imanishi et al. 2006a; Imanishi 2006; Imanishi et al. 2007; Armus et al. 2007; Imanishi et al. 2008; Nardini et al. 2008; Veilleux et al. 2009; Imanishi 2009; Nardini et al. 2009; Imanishi et al. 2010a,b; Nardini et al. 2010). Such infrared spectroscopy with high-spatial-resolution is, in principle, useful for dual AGN searches, but in practice, its application to faint AGNs in secondary galaxy nuclei is limited by spectroscopic sensitivity.

However, these infrared spectroscopic observations have clearly shown that the infrared 2–5 μm continuum emission in AGNs is systematically redder than the emission from starbursts (Imanishi et al. 2008; Sani et al. 2008; Risaliti et al. 2010; Imanishi et al. 2010b). The radiative energy generation efficiency of an AGN (= mass accreting SMBH; 6–42% of Mc^2) (Bardeen 1970; Thorne 1974) is much higher than that of a starburst (= nuclear fusion reaction inside stars; $\sim 0.7\%$ of Mc^2). Thus, high luminosity can be generated from a very compact region in an AGN. A larger amount of dust in the close vicinity (<10 pc) of an AGN can be heated to high temperatures with several 100 K (Barvainis 1987), producing stronger infrared L' -band (3.8 μm) radiation than a starburst whose infrared 2–5 μm flux is usually dominated by stellar photospheric blue emission. Observationally, pure AGNs are known to display strong L' -band flux excess relative to the K -band (2.2 μm) ($K - L' > 2.0$) (Ivanov et al. 2000; Alonso-Herrero et al. 2003; Videla et al. 2013), when compared to starburst activity ($K - L' \sim 0.5$) (Hunt et al. 2002). Hence, we can scrutinize dual AGNs, including deeply buried ones, through the detection of spatially compact red $K - L'$ sources. An important point is that while simple high-spatial-resolution imaging observations at wavelengths shorter than the K -band often cannot easily differentiate AGNs from compact starbursts for spatially compact emission at the distance of interesting gas- and dust-rich merging galaxies (Scoville et al. 2000), high-spatial-resolution imaging at both K and L' can better distinguish between AGNs and compact starbursts by combining morphological and color information. More importantly, this infrared *imaging* method is more sensitive than the infrared *spectroscopic* method and thus is applicable to a larger number of fainter secondary nuclei of gas- and dust-rich merging galaxies, which is crucial for dual AGN studies. Given that the ratio of infrared dust extinction to X-ray absorption (dust + gas) toward obscured AGNs is empirically known to be much smaller than the Galactic value

(Alonso-Herrero et al. 1997; Granato et al. 1997; Fadda et al. 1998; Georgantopoulos et al. 2012), the infrared K and L' -band observations could be sensitive even to Compton-thick buried AGNs, as was demonstrated in some sources (Imanishi & Dudley 2000; Imanishi et al. 2006a; Teng et al. 2005; Imanishi et al. 2008; Teng et al. 2009), making the infrared K - and L' -band imaging method particularly promising.

The recent availability of laser-guide-star adaptive optics (LGS-AO) on ground-based 8–10-m telescopes has enabled us to routinely achieve spatial resolutions of $<0''.2$ in infrared K - and L' -band images for the bulk of extra-galactic sources. Theoretical simulations of gas- and dust-rich galaxy mergers (Hopkins et al. 2005, 2006; van Wassenhove et al. 2012) predict that dual AGNs become luminous, particularly at the late merging stage, at separations of less than a few kiloparsecs. This physical separation corresponds to $<1''$ at $z > 0.1$, so sub-arcsecond resolution observations are crucial. The AO-assisted infrared K - and L' -band imaging method has several advantages: (1) it has even better spatial resolution ($<0''.2$) than the Chandra X-ray Observatory has ($\sim 0''.5$); (2) it is sensitive to buried AGNs with face-on SMBH orbits, which are missed in the previously employed optically based searches; and (3) it can trace radio-quiet AGNs. All of these qualities make this an excellent and unique method for a systematic search for dual AGNs in gas- and dust-rich merging galaxies. We have thus embarked on AO-assisted infrared K - and L' -band imaging observations of nearby gas- and dust-rich galaxy mergers using the Subaru 8.2-m telescope atop Mauna Kea, Hawaii. This is one of the best sites in the world for conducting highly sensitive L' -band observations, due to high elevation (~ 4200 m) and the resulting very low precipitable water vapor value.

Throughout this paper, we adopt $H_0 = 71 \text{ km s}^{-1} \text{ Mpc}^{-1}$, $\Omega_M = 0.27$, and $\Omega_\Lambda = 0.73$ (Komatsu et al. 2009). The luminosity distance is calculated using the cosmological calculator created by Wright et al. (2006). In Section 2, we describe our sample population. In Section 3, we present our observations and data analysis, followed by results in Section 4. We discuss the implications of our results in Section 5, and conclude with a summary of our work in Section 6.

2. TARGET SELECTION

We primarily target luminous infrared galaxies (LIRGs) whose infrared luminosities exceed $L_{\text{IR}} > 10^{11} L_\odot$ because they are a representative sample of gas- and dust-rich galaxy mergers in the local universe (Sanders & Mirabel 1996). In gas-rich LIRGs, it is expected that many SMBHs are mass accreting and so the detection rate of multiple SMBHs through luminous AGN searches is higher than in gas-poor galaxy mergers.

Previous systematic infrared spectroscopy revealed that buried AGNs play an increasing energetic role with increasing galaxy infrared luminosity and become particularly important in ultraluminous infrared galaxies (ULIRGs) with $L_{\text{IR}} > 10^{12} L_\odot$ (Imanishi 2009; Veilleux et al. 2009; Imanishi et al. 2010a,b; Nardini et al. 2010). Thus, ULIRGs are of particular interest. Among AGN-hosting ULIRGs at the brightest nuclei, those with spatially resolved multiple nuclei in seeing-limited images (Kim et al. 2002) are our first targets because investigat-

ing the presence of AGNs in the fainter secondary nuclei is a straightforward way to search for dual AGNs. In addition to these, we also include apparently single-nucleus ULIRGs in seeing-limited images because it may be possible to detect closely separated dual AGNs in our high-spatial-resolution AO images. Multiple-nuclei merging ULIRGs without strong AGN signatures in the brightest main nuclei are also added to see whether AGNs exist in the fainter secondary nuclei.

In addition to ULIRGs, we include five LIRGs for which previous 2–10 keV X-ray observations have suggested the presence of dual AGNs (Komossa et al. 2003; Bianchi et al. 2008; Piconcelli et al. 2010; Koss et al. 2011; Fabbiano et al. 2011). Our aim in including these targets in our sample is to confirm that dual AGN signatures could be found using our infrared K - and L' -band imaging method.

In total, 29 merging systems were observed, and their basic properties are summarized in Table 1. Our sample is neither homogeneous nor complete in a statistical sense. Our goal is to determine whether our infrared method, sensitive to buried AGNs, results in a substantially higher fraction of dual AGN detections than previous optically based methods, and to investigate whether the observed dual AGN fraction approaches unity, as predicted by theories, in gas- and dust-rich merging galaxies in the local universe.

3. OBSERVATION AND DATA ANALYSIS

We used the IRCS infrared camera and spectrograph (Kobayashi et al. 2000) at the Nasmyth focus of the Subaru 8.2-m telescope atop Mauna Kea, Hawaii (Iye et al. 2004), together with the 188-element adaptive optics (AO) system, using laser-guide stars (LGS) or natural-guide stars (NGS) (Hayano et al. 2008, 2010). For the LGS-AO to work properly, we need to find a star or compact object brighter than 18–19 mag in the optical R -band within $\sim 90''$ from the target to use as a guide star for good tip-tilt correction. The AO correction itself is made using a laser spot with an optical R -band magnitude of ~ 10.5 mag. Because most extra-galactic sources have such guide stars, we can now routinely obtain high-quality LGS-AO images with significantly improved image sizes compared with seeing-limited observations. When laser launch was possible, we performed LGS-AO observations. However, when it was not, we adopted NGS-AO observations. To achieve good NGS-AO performance, we need a star or compact source brighter than 16.5 mag in the optical R -band within $\sim 30''$ from the target to serve a guide star for AO correction. The number of external galaxies with such suitable NGS-AO guide stars is limited. Table 2 tabulates our observations, including information on guide stars used to achieve good AO performance and standard stars for photometric calibration. In summary, NGS-AO was used during the observing runs in 2011 June and 2013 May, and LGS-AO was adopted for all the remaining observing runs.

During our Subaru AO observations, the sky was clear. The seeing in the K -band ($2.2 \mu\text{m}$), measured in images before starting actual AO exposures, was $0''.3$ – $0''.7$ in full width at half maximum (FWHM). The precipitable water vapor value was low at <1 mm for the 2012 May run, <2 mm for 2011 June and July and 2012 October

runs, and ~ 3 mm for 2012 March and April and 2013 May runs; however, it was high at 4–5 mm for the 2011 August run.

In the K -band, we employed the 52 mas (52.77 mas pixel⁻¹) imaging mode to observe simultaneously some widely separated multiple galaxy nuclei and as many stars as possible to probe the point-spread function, within the field of view of $54''.04 \times 54''.04$ (1024 pixels \times 1024 pixels). The only exception is Mrk 231, which has very bright nuclear emission, for which we employed the 20 mas (20.57 mas pixel⁻¹) imaging mode to scatter the bright nuclear glare into many pixels and avoid array saturation. In the L' -band, as Earth's atmospheric background emission is high, we used the 20 mas imaging mode, whose field of view is $21''.06 \times 21''.06$ in the full-array mode. Even using this 20 mas mode, we had to use a sub-array mode to avoid saturating the array for the L' -band observations of some sources.

For the K -band observations of target merging (U)LIRGs, the exposure times were 0.26–30 sec, and 2–120 coadds were applied. In the L' -band, the exposure times were 0.076–0.12 sec, with 250–300 coadds. The individual exposure time was set so that signal levels at the object positions were below the linearity level of the IRCS imaging array (< 4000 ADU). Exposure times were dependent on the condition of Earth's atmosphere and on the ambient background emission level at the time of observations, as well as on the brightness of the object nuclei.

For target merging (U)LIRGs, we adopted nine-point dithering patterns to observe objects at nine different array positions and to overcome the effects of bad pixels. One dataset consisted of the nine dithered frames. For faint (U)LIRGs, this nine-point dithering pattern was repeated multiple times. The only exception was the IRAS 16474+3430 K -band data taken in 2011 July, for which a five-point dithering pattern was employed.

For all observing runs, photometric K - and L' -bands standard stars (Table 2) were observed, with a mean airmass difference of < 0.2 in directions similar to the individual (U)LIRGs to correct for the transmission of Earth's atmosphere at the time of observations and to provide a flux calibration. For standard star observations, NGS-AO was used whenever possible, using the standard stars themselves as AO guide stars to confirm the performance of the Subaru AO using point sources and to observe the stability and variation in the point-spread function under varying Earth atmospheric conditions. For a few very bright standard stars, we performed non-AO observations so that the signals did not exceed the linearity level of the IRCS array. For a few standard stars, we did not have enough time to optimize the AO parameters and so used AO without the best tuning. These data are useful for photometry but not for investigating the point-spread function.

Standard data analysis procedures were employed using IRAF². We first inspected the individual frames by eye. A very small fraction of frames showed strange patterns compared with the majority of the remaining nor-

mal frames. These strange frames were discarded from our analysis. We created median-combined sky frames to make a sky flat image for each dataset. In this procedure, the positions of bright objects and bad pixels were masked. Individual frames were sky-subtracted and divided by the sky flat frames for flat fielding. When the effects of cosmic ray hits and bad pixels remained for a few pixels at this stage, we made corrections manually by replacing the signals of these pixels with the interpolated values of the surrounding pixels. Then, we shifted the sky-subtracted, flat-fielded images so that the peak position of each target object landed on the same array pixel. For images that contained sufficiently bright compact sources inside the field of view of individual frames, the pixel shift was determined using these bright compact sources. The K -band frames often contained such sources. For a small fraction of the K -band data and the majority of the L' -band data, however, no such bright compact sources were seen in individual frames. In those cases, we used the offset values calculated from the dithering amplitude and pixel scale. We then average-combined these shifted frames to obtain final images. Based on a comparison of the FWHM values of compact objects between the resulting combined images and individual frames, we found this offset estimate to be very accurate for our AO data, due to the good quality of the AO guiding of the Subaru telescope.

4. RESULTS

4.1. K - and L' -band images

Figure 1 presents the infrared K - and L' -band AO images of the observed (U)LIRG nuclei. The achieved image sizes for stars and compact sources are usually $0''.1$ – $0''.2$ in FWHM both in the K - and L' -bands. Due to the higher atmospheric background emission, the sensitivity in the L' -band is much lower (worse) than that in the K -band. Consequently, the detection significance in the L' -band should be much lower than that in the K -band, unless the sources are very red in $K - L'$. In Figure 1, the detection rate of merging (U)LIRG nuclei is smaller in the L' -band than in the K -band, and yet a significant fraction of the observed merging nuclei are clearly detected in our highly sensitive L' -band AO images.

In the L' -band, the background emission for space-based infrared satellites is much lower than that for ground-based telescopes. So, as far as the detection of a single source is concerned, observations using space-based infrared satellites with small apertures could also be useful. WISE (40 cm) and Spitzer (75 cm) infrared satellites have imaging capabilities at $3.4 \mu\text{m}$ (Wright et al. 2010) and $3.6 \mu\text{m}$ (Fazio et al. 2004), respectively. These wavelengths are similar to our L' -band ($3.8 \mu\text{m}$). However, the spatial resolution of WISE at $3.4 \mu\text{m}$ and Spitzer at $3.6 \mu\text{m}$ are $\sim 6''.1$ (Wright et al. 2010) and $\sim 1''.7$ (Fazio et al. 2004), respectively. As our primary scientific goal is to locate closely-spaced dual AGNs and unveil their properties, higher-spatial-resolution ground-based AO images are more effective. As illustrative examples, Figure 2 compares our AO images of two ULIRGs at L' (Arp 220 and IRAS 16474+3430) with Spitzer IRAC camera images at $3.6 \mu\text{m}$ analyzed from archival data. Whereas multiple nuclei are clearly resolved in our AO images, the nuclei are not resolved in the Spitzer IRAC data. It is clear that our ground-based AO images are

² IRAF is distributed by the National Optical Astronomy Observatories, which are operated by the Association of Universities for Research in Astronomy, Inc. (AURA), under cooperative agreement with the National Science Foundation.

better for our scientific purpose.

4.2. Photometric aperture size

K - and L' -band emission originating from buried AGNs are dominated by AGN-heated hot dust located in the innermost part (<10 pc in physical scale or $<0''.1$ at $z > 0.01$) of the surrounding dusty material, and so are expected to be almost point sources. Higher-spatial-resolution photometry can minimize the contamination from spatially extended stellar-origin emission in host galaxies. In this regard, AO images have an advantage over seeing-sized non-AO images; the higher fraction of signal from compact sources is concentrated on a smaller central region. In our AO data, the measured image sizes of stars and compact galaxy nuclei are usually $0''.1$ – $0''.2$ in FWHM. However, we should note that in ground-based AO imaging data, even though the peak signal level of a compact source is higher than that in non-AO data, a considerable fraction of emission from a compact source spreads over a seeing-sized halo outside the AO core. The signal fraction within the AO core ($0''.1$ – $0''.2$ in FWHM) is usually significantly less than unity at $<4 \mu\text{m}$ (Minowa et al. 2010, 2012) and varies depending on the brightness of guide stars used for the LGS-AO tip-tilt correction or NGS-AO correction, their separation from the target objects, and Earth’s atmospheric turbulence at the time of observations. Hence, if we extract signal only from the AO-core emission component ($0''.1$ – $0''.2$ in FWHM), we will recover, for example, 50% of the spatially unresolved compact source flux in some cases and 75% in other cases. This difference will introduce a large uncertainty in the photometry of the nuclear compact sources among different galaxies. Larger aperture photometry can obviously cover a larger signal fraction of compact sources, but at the same time, the contamination from spatially extended stellar emission will increase. We must find the optimum aperture size such that the bulk of the compact source signal is covered, and yet the contamination from stellar emission is minimal.

Figure 3 plots the growth of the curves of the encircled signal in the L' -band using standard stars and a compact ULIRG observed with NGS-AO. Figure 4 displays the same plot for any compact sources found in the science target data, observed with LGS-AO. Although AO performance varies slightly among the different observing runs, 85–93% of total signal is usually recovered using a $\sim 0''.5$ ($25 \text{ pixels} \times 20.57 \text{ mas pixel}^{-1}$)-radius aperture. Even in the data taken in 2012 October, when seeing was most unstable among our observing runs in Table 2, $>83\%$ of the total signal is included within the selected aperture size. Thus, with the $\sim 0''.5$ radius aperture, we can consistently recover 83–93% of the spatially unresolved compact source flux in our L' -band LGS- and NGS-AO data.

Figure 5 shows the growth of the curves of the encircled signal in the K -band for standard stars and one ULIRG observed with NGS-AO. Figure 6 displays the same plot for any compact sources detected inside the science target frames taken with LGS-AO. In the K -band, Earth’s atmospheric turbulence effects are larger than in the L' -band. Also, the selected standard stars are generally fainter in the optical R -band than the L' -band standard stars. Thus, poorer growth of curves may be anticipated, and yet 75–90% of signals are usually recovered with the

$\sim 0''.5$ -radius aperture in the K -band.

For L' -band data, a standard star was observed with and without NGS-AO on the same night (2011 August 22 UT) (Figure 3, upper left). The AO data provide higher encircled signals at small radii than non-AO data, demonstrating the merit of AO for spatially unresolved compact source photometry using a small aperture.

From the fact that 75–90% and 83–93% of the spatially unresolved compact source signals are consistently recovered with a $\sim 0''.5$ -radius aperture in K - and L' -band data, respectively, taken on different nights, under different Earth’s atmospheric conditions, and with different guide star properties, we can safely conclude that Subaru AO, including both NGS-AO and LGS-AO, can provide such stable data, as long as the AO correction performs sufficiently well. We thus apply the same aperture size ($\sim 0''.5$ radius) for the photometry of nuclear compact sources (= hot dust emission heated by the putative AGNs) in the target (U)LIRGs and consider that 75–90% and 83–93% of compact source signal is recovered in the K - and L' -band, respectively. Table 3 summarizes the photometric measurements of individual merging nuclei using a $\sim 0''.5$ -radius aperture. The measurements are performed by varying the regions selected for sky subtraction, but are usually found to agree within much better than 0.2 mag.

The more significant source of photometric uncertainty is the slight variation in compact source signal fraction within the $\sim 0''.5$ -radius aperture. For example, if two different galaxies included 75% and 90% of the compact source signal, respectively, for the selected $\sim 0''.5$ -radius aperture, then the measured photometry could differ by ~ 0.2 mag between these sources, even if the intrinsic compact source flux were the same. Also, for the same galaxy nucleus, if 75% and 93% of compact source signal were included with the $\sim 0''.5$ -radius aperture in the K -band and L' -band, respectively, the derived $K - L'$ color could differ from the actual color by ~ 0.2 mag. Therefore, we must be aware that the ~ 0.2 mag photometric uncertainty among different galaxy nuclei or between the K - and L' -bands for the same galaxy nucleus is unavoidable in our AO photometry of spatially unresolved compact emission. In general, since the signal fraction of compact emission within the $\sim 0''.5$ -radius aperture is higher in the L' - than in the K -band (Figures 3–6), the estimated $K - L'$ colors can be at most ~ 0.2 mag redder than the true colors of the compact sources. The uncertainty in the $K - L'$ colors of compact source emission in a redder sense is reduced somewhat by the fact that the spatially extended stellar contribution to an observed flux (within the $\sim 0''.5$ -radius aperture) is higher in the K - than in the L' -band. This partially compensates for the slightly higher missing flux of compact source emission in the K - than in the L' -band. In summary, the measured $K - L'$ colors of spatially compact source emission should agree with the true colors within no redder than 0.2 mag.

As to the absolute flux of the compact source emission, the uncertainty is different from that of the $K - L'$ color. While our $\sim 0''.5$ -radius aperture recovers 75–90% and 83–93% of spatially unresolved compact source signals in the K - and L' -bands, respectively, a $\sim 2''$ -radius aperture is basically used for the photometry of AO-corrected standard stars (point sources with virtually no spatially ex-

tended emission) to recover as much point source signal as possible (>95%). Thus, when the $\sim 0''.5$ -radius aperture photometry of merging nuclei is compared with the $\sim 2''$ -radius aperture photometry of standard stars, the K - and L' -band compact source fluxes of merging galaxy nuclei could be underestimated by as much as ~ 0.3 mag (the maximum difference between 75–90% and 100%) in the K -band and ~ 0.2 mag (the maximum difference between 83–93% and 100%) in the L' -band. Table 4 compares our nuclear $0''.5$ -radius ($1''.0$ diameter) K -band photometry, with $1''.1$ diameter $2.2 \mu\text{m}$ photometry by Scoville et al. (2000) for (U)LIRG nuclei observed by both groups. Our photometry tends to be fainter by a few tenths of a magnitude, most likely because our aperture is slightly smaller, and some fraction of the seeing-sized AO halo signal of compact source emission is not covered. Hence, our AO photometry should not miss the spatially compact emission from the putative AGNs with more than ~ 0.3 mag in the K -band and ~ 0.2 mag in the L' -band, which will not affect our main discussions and conclusions.

5. DISCUSSION

5.1. Galaxy nuclei with luminous detectable AGNs

As mentioned in the introduction, AGNs should have redder $K - L'$ colors than starbursts due to the larger amount of hot (several 100 K) dust emission in the former. Although the intrinsic $K - L'$ colors could have some scatter for individual starbursts and AGNs, we adopt the values for intrinsic $K - L'$ color = 0.5 mag for starburst activity (Hunt et al. 2002) and $K - L' = 2.0$ mag for AGNs (Ivanov et al. 2000; Alonso-Herrero et al. 2003; Videla et al. 2013). The observed $K - L'$ colors vary as a function of the AGN contribution to the observed flux, increasing (reddening) with increasing AGN contribution. Our calculation shows that the $K - L'$ color becomes > 1.0 mag when the AGN contribution to the L' -band flux exceeds $\sim 50\%$. Hence, for the purposes of this analysis, we consider that galaxy nuclei with $K - L' \gtrsim 1.0$ mag contain luminous recognizable AGNs rather than an intrinsic color scatter of starbursts. Based on Table 3 (column 4), at least one AGN ($K - L' \gtrsim 1.0$ mag) is detected with our AO-assisted infrared imaging method in all sources except IRAS 21208–0519, demonstrating that our method is very effective at detecting AGNs in many gas- and dust-rich merging (U)LIRG nuclei. In Table 3 (column 5), the estimated AGN contribution to the observed L' -band flux is shown for (U)LIRG nuclei with $K - L' = 0.5$ – 2.0 mag. (U)LIRG nuclei with $K - L' < 0.5$ mag and > 2.0 mag are taken as 100% dominated by starbursts and AGNs, respectively.

We now comment on some strengths of our method and discuss some caveats. First, the infrared L' -band is very sensitive to an AGN. Assuming the typical spectral energy distribution of an AGN and a starburst, the L' -band-to-bolometric luminosity ratio of an AGN (~ 0.2) is two orders of magnitude higher than that of a starburst (~ 0.002) (Risaliti et al. 2010). This means that for an AGN whose bolometric contribution is only 10% (5%), as much as 91% (84%) of the observed infrared L' -band flux comes from the AGN (no dust extinction case). Even if the dust extinction of a buried AGN is larger by $A_V \sim 35$ mag than the surrounding starbursts, 52% (34%) of the infrared L' -band flux originates in the buried AGN, if

we adopt the dust extinction curve derived by Nishiyama et al. (2008, 2009). In short, we should be able to detect moderately luminous buried AGNs even in galaxies with coexisting strong starbursts. This is likely to be the primary reason that our method allows the detection of many AGNs in the gas- and dust-rich merging (U)LIRGs that usually accompany strong starburst activity.

Next, we discuss an alternative possible mechanism for increasing $K - L'$ colors. Dust extinction can redden the colors of obscured starbursts. If the $K - L'$ colors become $\gtrsim 1.0$ mag by this mechanism without invoking AGN-heated hot dust emission, some galaxy nuclei with $K - L' > 1.0$ mag may not contain luminous AGNs. However, recent observations have shown that the dust extinction curve is relatively flat in the infrared K - and L' -band wavelength range, with dust extinction at L' only 0.5–0.7 times the extinction at K ($A_{L'} = 0.5$ – $0.7 \times A_K$) (Nishiyama et al. 2008, 2009; Gao et al. 2009). Adopting $A_K/A_V = 0.062$ (Nishiyama et al. 2008), even in the case of dust extinction as large as $A_V = 10$ mag (foreground screen dust absorption case), the $K - L'$ colors change by only ~ 0.3 mag. In fact, in normal starburst galaxies, stellar energy sources and dust and gas are spatially well mixed (Puxley 1991; McLeod et al. 1993; Forster Schreiber et al. 2001), and the actual flux attenuation should be much lower than the foreground screen dust model for the same dust extinction toward the most dust-obscured region at the other side. Hence, we anticipate that a color reddening of starbursts to $K - L' \gtrsim 1.0$ mag by dust extinction is not very common, and therefore that $K - L' \gtrsim 1.0$ mag nuclei are dominated by luminous hot-dust-emitting AGNs, with a very small contribution from highly obscured starburst nuclei.

Dust extinction for buried-AGN-heated hot dust emission could also alter the observed $K - L'$ colors. Given that the dust extinction of buried-AGN-heated K - and L' -band emitting hot dust in the inner part of the dusty envelope is most likely to be substantially larger than that in the surrounding starburst regions and that a foreground screen dust model is applied to buried AGNs (Imanishi et al. 2007), this effect may not be neglected. We now assume the dust extinction curve of $A_K/A_V = 0.062$ and $A_{L'}/A_V = 0.031$ derived by Nishiyama et al. (2008, 2009), and consider the two examples of $A_V = 16$ mag and $A_V = 32$ mag as dust extinction for the buried-AGN-heated hot dust emission. Flux attenuation of starburst-origin K - and L' -band emission by dust extinction is assumed to be negligible here. The buried-AGN-origin $K - L'$ colors change from 2.0 mag to 2.5 mag and 3.0 mag in the case of $A_V = 16$ mag and 32 mag, respectively, while the $K - L'$ colors of starbursts remain unchanged as 0.5 mag. In this case, the observed $K - L'$ colors become $\gtrsim 1.0$ mag, when the contributions from buried-AGN-origin emission to the observed L' -band fluxes are 44% and 41%, respectively, which are smaller than no dust extinction case for the AGN-heated hot dust emission ($\sim 50\%$ AGN contribution is required to make $K - L' \gtrsim 1.0$ mag). However, in the case of $A_V = 16$ mag and 32 mag dust extinction toward the buried-AGN-heated hot dust region, the intrinsic AGN-heated hot dust emission luminosities will increase by a factor of 1.6 and 2.5, respectively, after correction for the flux attenuation by dust extinction. When this correction is applied, the fraction of the intrinsic AGN-origin L' -band

flux, relative to the observed L' -band flux, becomes 55% and 64% for the $A_V = 16$ mag and 32 mag dust extinction case, respectively. These fractions are even larger than that in the case of no dust extinction for AGN-heated hot dust emission. Therefore, our argument that important AGN contributions are required to reproduce the observed colors of $K - L' \gtrsim 1.0$ mag will not change, or even be strengthened.

Now that the AGN contribution to the observed L' -band flux has been estimated (Table 3, column 5; no dust extinction case for the AGN-heated hot dust emission), we can derive the luminosity of the AGN-heated hot dust emission in the close vicinity (<10 pc) of an AGN, which dominates the AGN-originated L' -band flux. As our main targets are optically elusive buried AGNs surrounded by dust and gas with a covering factor close to unity, we here assume a simple spherical dust distribution. In this geometry, dust has a strong temperature gradient. Inner (outer) dust has a higher (lower) temperature, and dust emission luminosity is conserved at each temperature from the hot inner regions to the cool outer regions (Imanishi et al. 2007; Imanishi 2009). The inner hot dust should generate most of the L' -band ($3.8 \mu\text{m}$) emission, and the intrinsic AGN-origin L' -band luminosity (νL_ν or λL_λ), after subtracting the stellar contamination, should be as large as the intrinsic AGN UV–optical energetic radiation luminosity at the very center.

The estimated AGN luminosity is tabulated in Table 3 (column 6). This AGN luminosity is derived from the observed AGN-origin L' -band luminosity, with no dust extinction correction. Correction for possible dust extinction of the AGN-origin L' -band emission will increase the intrinsic AGN UV–optical energetic radiation luminosity. Additionally, if the dust covering factor around an AGN is substantially below unity, the AGN-heated hot dust emission luminosity underestimates the intrinsic AGN UV–optical energetic radiation luminosity. For these reasons, the derived AGN luminosity in our method should be taken as a lower limit.

5.2. Infrared properties of X-ray dual AGNs

Among the 29 observed infrared luminous merging systems, signatures of dual AGNs with separations of $>0''.5$ were previously reported from X-ray observations for the following five sources: Mrk 463 (Bianchi et al. 2008), Mrk 739 (Koss et al. 2011), NGC 3393 (Fabbiano et al. 2011), NGC 6240 (Komossa et al. 2003), and IRAS 20210+1121 (Piconcelli et al. 2010). Using our methods, we detect double nuclear emission in Mrk 463, Mrk 739, NGC 6240, and IRAS 20210+1121, but not in NGC 3393. However, only NGC 6240 displays the double red ($K - L' \gtrsim 1.0$ mag) nuclei that are indicative of a dual AGN. Mrk 463, Mrk 739, and IRAS 20210+1121 show only one red ($K - L' \gtrsim 1.0$ mag) nucleus, with a blue $K - L'$ color (<1.0 mag) at the other nucleus.

In NGC 3393, we see no signature of a secondary nucleus at $\sim 0''.6$ away from the primary nucleus (Fabbiano et al. 2011), although our AO images should be able to resolve both nuclei spatially. A similar case is found in an AGN at $z = 0.16$ (SDSS J171544.05+600835.7), in which double X-ray emission is found with the Chandra X-ray Observatory, but the infrared K -band image shows a single nuclear morphology (Comerford et al. 2011). However, no X-ray spectra are shown in this source, and the

origin of the detected X-ray emission is less clear than NGC 3393.

X-ray observations are sensitive to an AGN, irrespective of the presence of hot dust in the close vicinity of a mass-accreting SMBH, and our infrared imaging method requires the presence of hot dust for AGN detection. If the detected X-ray emission from both nuclei originates in luminous AGNs, one nucleus in Mrk 463, Mrk 739, NGC 3393, and IRAS 20210+1121 could be a hot-dust-deficient AGN, in which case the contribution from AGN-heated hot dust emission to the observed L' -band flux would be small, and the observed infrared K - and L' -band fluxes would be dominated by nuclear stellar-origin emission.

5.3. Fraction of infrared dual AGNs

Among the 29 observed merging (U)LIRGs, only four systems (Mrk 273, Arp 220, IRAS 16474+3430, and NGC 6240) show red ($K - L' \gtrsim 1.0$ mag) colors in both merging nuclei, indicative of dual AGNs. Thus, the fraction of detected dual AGNs is $\sim 14\%$ (4/29). Because the bottom five sources in Table 1 are known dual AGNs from previous X-ray observations, their inclusion could bias the fraction of detectable dual AGNs. However, only one out of the five sources ($=20\%$) is an infrared dual AGN, not significantly biasing the total dual AGN fraction. The detected dual AGN fraction in our infrared imaging method is apparently slightly higher than that of previous optical dual AGN surveys with $<5\%$ (Liu et al. 2010; Shen et al. 2011), although the sample size is still small, and the sample selection criteria are different. However, the detected dual AGN fraction is far below unity and is much smaller than the value expected from the simple prediction that the majority of gas- and dust-rich merging galaxies should have multiple active SMBHs.

Because our infrared imaging method is sensitive to buried AGNs, it is unlikely that the small detectable dual AGN fraction is due to the elusiveness of AGNs obscured by dust (see §1). Previous optical spectroscopic dual AGN searches and our method are sensitive to multiple active SMBHs with edge-on and face-on orbiting geometry, respectively, and the detectable dual AGN fraction is still much less than unity, even after combining these two methods. Thus, the most natural explanation is non-simultaneous SMBH activation (van Wassenhove et al. 2012). We can observationally identify the presence of SMBHs at the distance of the observed merging galaxies, only if the SMBHs are actively mass accreting. If only one of the multiple SMBHs is sufficiently active to be observationally detectable over the long time period of a galaxy merger, and if the phase during which both SMBHs are active is short, then most merging galaxies with multiple SMBHs cannot be identified as dual AGNs. This scenario predicts that the mass accretion rates onto SMBHs should be different for multiple SMBHs. To test this scenario, we compare the buried AGN luminosity, derived from our infrared observations, with K -band photometry, including host galaxy emission (Kim et al. 2002; Skrutskie et al. 2006), for spatially resolved multiple-nuclei merging systems in seeing-limited images. These K -band luminosities should reflect the stellar luminosity, and SMBH mass ratios in individual merging nuclei are expected to be roughly proportional

to the K -band stellar luminosity ratios (Marconi & Hunt 2003; Vika et al. 2012).

Figure 7 (Left) compares the K -band stellar luminosity ratio (i.e., SMBH mass ratio) and nuclear L' -band luminosity ratio (Table 5) between seeing-based spatially resolved multiple nuclei. If both SMBHs in multiple nuclei systems have similar mass accretion rates when normalized to the SMBH mass, then the sources are expected to be distributed around the solid line. However, most sources are located far from the solid line, suggesting that the mass accretion rates per SMBH mass (= Eddington ratio) are significantly different between the two nuclei in the majority of the observed multiple-nuclei merging systems. In Figure 7 (right), we also compare the K -band stellar luminosity ratio with AGN-origin L' -band luminosity ratio after subtracting stellar contamination. In Figure 7 (left) and (right), some ambiguity remains. In the left panel, stellar emission could contribute to the L' -band flux, whereas in the right panel, the AGN subtraction process could introduce some uncertainty. However, both plots show basically the same behavior: most sources largely deviate from the solid line, strongly suggesting that SMBH activation is non-synchronous. The bulk of the observed merging (U)LIRGs are distributed along the upper-left side of the solid line, indicating that larger-mass SMBHs generally have higher Eddington ratios than smaller-mass SMBHs.

In this comparison, we need to include some cautionary statements. First, the large-aperture K -band photometry could include emission from AGNs, particularly for luminous AGNs that are weakly obscured by dust. In these systems, AGN-origin nuclear emission could contribute substantially to the observed K -band flux. This might result in an overestimate of the inferred SMBH mass from the observed K -band luminosity. However, since our primary targets are obscured AGNs in gas- and dust-rich merging (U)LIRGs, this effect is not expected to be severe in most cases. In Figure 7, the bulk of the observed sources are distributed around the upper-left side of the solid line, a region in which larger SMBHs are more actively mass accreting (= higher Eddington ratios). The AGN contribution to the K -band flux can be high in such larger-mass SMBHs with high Eddington ratios if they are less dust obscured. If this effect is present in some sources, then the actual mass of the larger SMBH is smaller than our estimate. In that case, the true Eddington ratios in larger-mass SMBHs would become even higher, increasing the non-simultaneity of the mass-accretion rates onto multiple SMBHs. Thus, our main conclusion does not change.

Second, our method provides higher AGN luminosity in the L' -band brighter nucleus than in the L' -band fainter nucleus in each merging system because the possible dust extinction of AGN-heated hot dust emission is not taken into account. Assuming that the Eddington ratios are similar for SMBHs at two nuclei, if dust extinction of AGN-heated hot dust is generally smaller in the larger-mass SMBHs than in the smaller-mass SMBHs, then many sources would appear at the upper-left side of the solid line in Figure 7. The trends observed in Figure 7 could be reproduced without introducing non-synchronous SMBH mass accretion. Similar Eddington ratios would mean that larger-mass SMBHs have higher absolute mass accretion rates, requiring a larger amount

of fuel in the vicinity of the SMBHs, which could obscure the SMBHs. In gas- and dust-rich infrared luminous merging galaxies, more luminous AGNs with higher absolute mass accretion rates are predicted to be more highly obscured (Hopkins et al. 2006), making this second scenario (similar Eddington ratios with less dust extinction in the larger-mass SMBHs) unlikely, and still supporting the suggestion that larger-mass SMBHs have generally higher Eddington ratios.

Third, when we convert K -band stellar luminosity to SMBH mass, we need to mention that younger star formation is likely to have higher K -band luminosity than older star formation for a given galaxy stellar mass (Bell & de Jong 2001). The inferred SMBH mass can be overestimated for younger star formation. Actively mass-accreting SMBHs indicate the presence of dynamically settled nuclear gas, which is likely to cause active young nuclear starbursts (Imanishi 2002; Imanishi et al. 2003; Imanishi & Wada 2004; Oi et al. 2010; Imanishi et al. 2011a). Thus, the SMBH mass could be overestimated for active SMBHs with higher Eddington ratios. Now, Figure 7 suggests that larger-mass SMBHs have higher Eddington ratios in general than do smaller-mass SMBHs. If the abscissa is changed from K -band stellar luminosity to actual SMBH mass, many sources currently located around the upper-left side of the solid line in Figure 7 would move leftward, even strengthening the scenario that larger mass SMBHs have higher Eddington ratios. Thus, this uncertainty also will not change our conclusion.

Figure 8 plots the comparison of the nuclear L' -band to galaxy-wide K -band stellar luminosity ratio (Left) and AGN-origin L' -band to K -band stellar luminosity ratio (Right), between two nuclei, as a function of apparent nuclear separation. Since the K -band stellar luminosity is taken as the indicator of SMBH mass (Marconi & Hunt 2003; Vika et al. 2012), the ordinate corresponds to the ratio of SMBH-mass-normalized mass accretion rates (= Eddington ratio) between the two nuclei. Sources close to (far away from) the solid horizontal lines mean that SMBH-mass-normalized mass accretion rates are similar (largely different) between the two nuclei. If dual SMBH activation preferentially occurs at a later merging stage (van Wassenhove et al. 2012), it is expected that sources with small apparent nuclear separation tend to be distributed around the solid horizontal lines. No such trend is seen.

Finally, our comparison of SMBH mass and AGN luminosity above is limited to (U)LIRGs with spatially resolved nuclei in seeing-limited images. Multiple active closely-separated SMBHs ($<<1''$), which are spatially resolvable only with our AO images (e.g., IRAS 16474+3430 in Figure 1, L' -band image), are very interesting, in terms of the theoretical prediction that such SMBHs in the late stages of gas- and dust-rich galaxy mergers become particularly active and become luminous AGNs (Hopkins et al. 2005, 2006; van Wassenhove et al. 2012). However, although AGN luminosity ratios for closely separated systems could be derived from our AO-assisted high-spatial-resolution infrared K - and L' -band imaging data (Table 3), SMBH mass ratios are difficult to obtain from stellar emission luminosity in K -band images because host galaxy's stellar emission strongly overlaps between multiple nuclei. Spatially resolved veloc-

ity information obtained with AO-assisted spectroscopy will be useful for inferring SMBH ratios in such small-separation SMBH systems, but such observations are still limited to very bright nuclei only (Medling et al. 2011; U et al. 2013). Investigating the properties of these closely separated SMBHs requires additional future work.

In summary, our results support the scenario proposed by the theory (van Wassenhove et al. 2012) that SMBH mass accretion is not simultaneous among multiple SMBHs in gas- and dust-rich merging galaxies. In general, larger-mass SMBHs are more actively mass accreting (normalized to SMBH mass) in merging (U)LIRGs with multiple nuclei in seeing-limited images. This non-synchronous SMBH activation may reduce the fraction of observable dual AGN, compared to the fraction of multiple SMBHs, in merging galaxies. Our results suggest that mass accretion onto SMBHs is dominated by the local environment on the small scale rather than by global galaxy properties, even in gas- and dust-rich infrared luminous merging galaxies. In this case, it is not easy to predict SMBH activity through theoretical simulations of galaxy mergers. Thus, observations are important for understanding how multiple SMBHs are activated during the gas- and dust-rich galaxy merger process.

6. SUMMARY

We conducted infrared K - and L' -band high-spatial-resolution ($<0''.2$) imaging observations of nearby infrared luminous merging galaxies using Subaru LGS/NGS-AO to search for kiloparsec-scale multiple AGNs surrounded by dust through the detection of red $K-L'$ compact sources. Given the gas- and dust-rich nature of these galaxies, many SMBHs are expected to be mass accreting and hence to become luminous AGNs, but these AGNs are deeply buried in gas and dust. Using our infrared method, which is sensitive to buried AGNs, the observational detection of multiple SMBHs is expected to be more feasible than in gas-poor galaxy mergers where many SMBHs may not be actively mass accreting due to the paucity of surrounding gas. We present the following main conclusions.

1. Among 29 observed merging systems, at least one AGN was found in all sources except one, demonstrating the effectiveness of our method for the purpose of AGN detection in these gas- and dust-rich infrared luminous merging galaxies.
2. Kiloparsec-scale dual AGNs were seen in only four of 29 galaxies, even using our powerful method, which is sensitive to deeply buried AGNs. This fraction seems slightly higher than the fraction determined by previously published optical spectroscopic dual AGN searches, despite the small sample size and the differences in criteria used for sample selection. However, the fraction is still significantly smaller than the value derived from the simple theoretical prediction that most gas- and dust-rich merging galaxies are expected to contain multiple active SMBHs.
3. The AGN luminosity ratios derived from AGN-origin L' -band emission between two nuclei are, in most cases, higher than the SMBH mass ratios

inferred from large-aperture K -band photometric observations. When normalized to SMBH mass, larger-mass SMBHs are generally more highly mass accreting than are smaller-mass SMBHs in most of the observed infrared luminous merging galaxies with spatially resolved nuclei in seeing-limited images. This trend is independent of the apparent nuclear separation.

4. When combined with previous optically based dual AGN searches, our observational results suggest that the most likely reason for the small observed dual AGN fraction in merging galaxies is that mass accretion onto multiple SMBHs is non-simultaneous rather than the result of the orbiting geometry of multiple SMBHs or the optical elusiveness of AGNs deeply buried in gas and dust.
5. Our results suggest that in gas- and dust-rich infrared luminous merging galaxies, mass accretion onto SMBHs is primarily determined by local conditions rather than by global galaxy properties. This makes theoretical prediction difficult and necessitates the inclusion of observational constraints when attempting to understand what is happening for SMBHs in gas- and dust-rich galaxy mergers.

We thank the anonymous referee for his/her useful comment. We are grateful to Drs. Minowa and Ishii for their support during our observations at the Subaru Telescope and to Sayaka Yamaguchi for her English proofreading. M.I. is supported by a Grant-in-Aid for Scientific Research (23540273). This research made use of (1) the SIMBAD database, operated at CDS, Strasbourg, France, and the NASA/IPAC Extragalactic Database (NED) operated by the Jet Propulsion Laboratory, California Institute of Technology, under contract with the National Aeronautics and Space Administration, (2) data products from the Two Micron All Sky Survey, which is a joint project of the University of Massachusetts and the Infrared Processing and Analysis Center/California Institute of Technology, funded by the National Aeronautics and Space Administration and the National Science Foundation, and (3) the NASA/IPAC Infrared Science Archive, which is operated by the Jet Propulsion Laboratory, California Institute of Technology, under contract with the National Aeronautics and Space Administration.

REFERENCES

- Alonso-Herrero, A., Quillen, A. C., Rieke, G. H., Ivanov, V., & Efstathiou, A. 2003, *AJ*, 126, 81
- Alonso-Herrero, A., Ward, M. J., & Kotilainen, J. K. 1997, *MNRAS*, 288, 977
- Armus, L., Charmandaris, V., Bernard-Salas, J., et al. 2007, *ApJ*, 656, 148
- Balestra, I., Boller, T., Gallo, L., Lutz, D., & Hess, S. 2005, *A&A*, 442, 469
- Ballo, L., Braitto, V., Della Ceca, R., et al. 2004, *ApJ*, 600, 634
- Barvainis, R., 1987, *ApJ*, 320, 537
- Bardeen, J. M. 1970, *Nature*, 226, 64
- Barrows, R., Lacy, C. H. S., Kenefick, J., et al. 2013, *ApJ*, 769, 95
- Bell, E. F., & de Jong, R. S. 2001, *ApJ*, 550, 212
- Beswick, R. J., Pedlar, A., Mundell, C. G., Gallimore, J. F. 2001, *MNRAS*, 325, 151
- Bianchi, S., Chiaberge, M., Piconcelli, E., Guainazzi, M., & Matt, G. 2008, *MNRAS*, 386, 105
- Braitto, V., Della Ceca, R., Piconcelli, E., et al. 2004, *A&A*, 420, 79
- Burke-Spolaor, S. 2011, *MNRAS*, 410, 2113
- Colpi, M., & Dotti, M. 2011, *Advanced Science Letters*, 4, 181
- Comerford, J. M., Gerke, B. F., Stern, D., et al. 2012, *ApJ*, 753, 42
- Comerford, J. M., Pooley, D., Gerke, B. F., & Madejski, G. M. 2011, *ApJ*, 737, L19
- Dasyra, K. M., Tacconi, L. J., Davies, R. I., et al. 2006a, *ApJ*, 638, 745
- Dasyra, K. M., Tacconi, L. J., Davies, R. I., et al. 2006b, *ApJ*, 651, 835
- Diaz, A. I., Prieto, M. A., Wamsteker, W. 1988, *A&A*, 195, 53
- Downes, D., & Eckart, A. 2007, *A&A*, 468, L57
- Dudley, C. C., & Wynn-Williams, C. G. 1997, *ApJ*, 488, 720
- Fabbiano, G., Wang, J., Elvis, M., & Risaliti, G. 2011, *Nature*, 477, 431
- Fadda, D., Giuricin, G., Granato, G. L., & Vecchies, D. 1998, *ApJ*, 496, 117
- Farrah, D., Bernard-Salas, J., Spoon, H. W. W., et al. 2007, *ApJ*, 667, 149
- Fazio, G. G., Hora, J. L., Allen, L. E., et al. 2004, *ApJS*, 154, 10
- Ferrarese, L., & Merritt, D. 2000, *ApJ*, 539, L9
- Forster Schreiber, N. M., Genzel, R., Lutz, D., Kunze, D., & Sternberg, A. 2001, *ApJ*, 552, 544
- Fu, H., Myers, A., Djorgovski, S. G., & Yan, L. 2011, *ApJ*, 733, 103
- Fu, H., Yan, L., Myers, A., et al. 2012, *ApJ*, 745, 67
- Gallimore, J. F., & Beswick, R. 2004, *AJ*, 127, 239
- Gao, J., Jiang, B. W., & Li, A. 2009, *ApJ*, 707, 89
- Ge, J.-Q., Hu, C., Wang, J.-M., Bai, J.-M., & Zhang, S. 2012, *ApJS*, 201, 31
- Georgantopoulos, I., Dasyra, K. M., Rovilos, E., et al. 2011, *A&A*, 531, 116
- Goldschmidt, P., Kukula, M. J., Miller, L., & Dunlop, J. S. 1999, *ApJ*, 511, 612
- Granato, G. L., Danese, L., & Franceschini, A. 1997, *ApJ*, 486, 147
- Gultekin, K., Richstone, D. O., Gebhardt, K., et al. 2009, *ApJ*, 698, 198
- Harrison, F. A., Craig, W. W., Christensen, F. E., et al. 2013, *ApJ*, 770, 103
- Hayano, Y., Takami, H., Guyon, O., et al. 2008, *SPIE*, 7015, 25
- Hayano, Y., Takami, H., Oya, S., et al. 2010, *SPIE*, 7736, 21
- Hopkins, P. F., Hernquist, L., Cox, T. J., et al. 2005, *ApJ*, 630, 705
- Hopkins, P. F., Hernquist, L., Cox, T. J., et al. 2006, *ApJS*, 163, 1
- Hunt, L. K., Giovanardi, C., & Helou, G. 2002, *A&A*, 394, 873
- Hutchings, J. N., & Neff, S. G. 1989, *AJ*, 97, 1306
- Imanishi, M. 2002, *ApJ*, 569, 44
- Imanishi, M. 2003, *ApJ*, 599, 918
- Imanishi, M. 2006, *AJ*, 131, 2406
- Imanishi, M. 2009, *ApJ*, 694, 751
- Imanishi, M., & Dudley, C. C. 2000, *ApJ*, 545, 701
- Imanishi, M., Dudley, C. C., & Maloney, P. R. 2001, *ApJ*, 558, L93
- Imanishi, M., Dudley, C. C., & Maloney, P. R. 2006a, *ApJ*, 637, 114
- Imanishi, M., Dudley, C. C., Maiolino, R., et al. 2007, *ApJS*, 171, 72
- Imanishi, M., Ichikawa, K., Takeuchi, T., et al. 2011a, *PASJ*, 63, S447
- Imanishi, M., Imase, K., Oi, N., & Ichikawa, K. 2011b, *AJ*, 141, 156
- Imanishi, M., Maiolino, R., & Nakagawa, T. 2010a, *ApJ*, 709, 801
- Imanishi, M., Nakagawa, T., Ohshima, Y., et al. 2008, *PASJ*, 60, S489
- Imanishi, M., Nakagawa, T., Shirahata, M., Ohshima, Y., & Onaka, T. 2010b, *ApJ*, 721, 1233
- Imanishi, M., & Terashima, Y. 2004, *AJ*, 127, 758
- Imanishi, M., Terashima, Y., Anabuki, N., & Nakagawa, T. 2003, *ApJ*, 596, L167
- Imanishi, M., & Wada, K. 2004, *ApJ*, 617, 214
- Itoh, T., Done, C., Makishima, K., et al. 2008, *PASJ*, 60, S251
- Ivanov, V. D., Rieke, G. H., Groppi, C. E., et al. 2000, *ApJ*, 545, 190
- Iye, M., Karoji, H., Ando, H., et al., 2004, *PASJ*, 56, 381
- Iwasawa, K., Mazzarella, J. M., Surace, J. A., et al. 2011a, *A&A*, 528, 137
- Iwasawa, K., Sanders, D. B., Teng, S. H., et al. 2011b, *A&A*, 529, 106
- Kim, D. -C., & Sanders, D. B. 1998, *ApJS*, 119, 41
- Kim, D. -C., Veilleux, S., & Sanders, D. B. 2002, *ApJS*, 143, 277
- Kobayashi, N., Tokunaga, A. T., Terada, H., et al. 2000, *IRCS: Infrared camera and spectrograph for the Subaru Telescope*, in *Proc. SPIE 4008: Optical and IR Telescope Instrumentation and Detectors*, eds M. Iye & A. F. Moorwood, 1056
- Komatsu, E., Dunkley, J., Nolte, M. R., et al. 2009, *ApJS*, 180, 330
- Komossa, S., Burwitz, V., Hasinger, G., et al. 2003, *ApJ*, 582, L15
- Koss, M., Mushotzky, R., Treister, E., et al. 2011, *ApJ*, 735, L42
- Koss, M., Mushotzky, R., Treister, E., et al. 2012, *ApJ*, 746, L22
- Liu, X., Civano, F., Shen, Y., et al. 2013, *ApJ*, 762, 110
- Liu, X., Shen, Y., Strauss, M., Greene, J. E. 2010, *ApJ*, 708, 427
- Liu, X., Shen, Y., Strauss, M. A., & Hao, L. 2011, *ApJ*, 737, 101
- Magorrian, J., Tremaine, S., Richstone, D., et al. 1998, *ApJ*, 115, 2285
- Maiolino, R., Comastri, A., Gilli, R., et al. 2003, *MNRAS*, 344, L59
- Maloney, P. R., & Reynolds, C. S. 2000, *ApJ*, 545, L23
- Marconi, A., & Hunt, L. K. 2003, *ApJ*, 589, L21
- Max, C. E., Canalizo, G., & de Vries, W. H. 2007, *Science*, 316, 1877
- McConnell, N. J. & Ma, C-P. 2013, *ApJ*, 764, 184
- McLeod, K. K., Rieke, G. H., Rieke, M. J., & Kelly, D. M. 1993, *ApJ*, 412, 111
- Medling, A. M., Ammons, S. M., Max, C. E., et al. 2011, *ApJ*, 743, 32
- Minowa, Y., Hayano, Y., Oya, S., et al. 2010, *SPIE*, 7736, 77363N
- Minowa, Y., Hayano, Y., Terada, H., et al. 2012, *SPIE*, 8447, 84471F
- Moorwood, A. F. M. 1986, *A&A*, 166, 4
- Nardini, E., Risaliti, G., Salvati, M., et al. 2008, *MNRAS*, 385, L130
- Nardini, E., Risaliti, G., Salvati, M., et al. 2009, *MNRAS*, 399, 1373
- Nardini, E., Risaliti, G., Watabe, Y., Salvati, M., & Sani, E. 2010, *MNRAS*, 405, 2505
- Nishiyama, S., Nagata, T., Tamura, M., et al. 2008, *ApJ*, 680, 1174
- Nishiyama, S., Tamura, M., Hatano, H., et al. 2009, *ApJ*, 696, 1407
- Oi, N., Imanishi, M., & Imase, K. 2010, *PASJ*, 62, 1509
- Perez, E., Manchado, A., Garcia-Lario, P., & Pottash, R. 1990, *A&A*, 227, 407
- Piconcelli, E., Vignali, C., Bianchi, S., et al. 2010, *ApJ*, 722, L147
- Pilyugin, L. S., Zinchenko, I. A., Cedres, B., et al. 2012, *MNRAS*, 419, 490
- Puxley, P. J. 1991, *MNRAS*, 249, 11p
- Ranalli, P., Comastri, A., & Setti, G. 2003, *A&A*, 399, 39
- Risaliti, G., Gilli, R., Maiolino, R., & Salvati, M. 2000, *A&A*, 357, 13
- Risaliti, G., Imanishi, M., & Sani, E. 2010, *MNRAS*, 401, 197
- Rodriguez, C., Taylor, G. B., Zavala, R. T., et al. 2006, *ApJ*, 646, 49

- Rosario, D. J., McGurk, R. C., Max, C. E., et al. 2011, *ApJ*, 739, 44
- Ryter, C. E. 1996, *ApSS*, 236, 285
- Sanders, D. B., & Mirabel, I. F. 1996, *ARA&A*, 34, 749
- Sanders, D. B., Soifer, B. T., Elias, J. H., Neugebauer, G., & Matthews, K. 1988, *ApJ*, 328, L35
- Sani, E., Risaliti, G., Salvati, M., et al. 2008, *ApJ*, 675, 96
- Scoville, N. Z., Evans, A. S., Thompson, R., et al. 2000, *AJ*, 119, 991
- Severgnini, P., Risaliti, G., Marconi, A., Maiolino, R., & Salvati, M. 2001, *A&A*, 368, 44
- Shang, Z., Brotherton, M. S., Wills, B. J., et al. 2011, *ApJ*, 196, 2
- Shen, Y., Liu, X., Greene, J. E., & Strauss, M. A. 2011, *ApJ*, 735, 48
- Shuder, J. M., & Osterbrock, D. E. 1981, *ApJ*, 250, 55
- Skrutskie, M. F., Cutri, R. M., Stiening, R., et al. 2006, *AJ*, 131, 1163
- Smith, K. L., Shields, G. A., Bonning, E. W., et al. 2010, *ApJ*, 716, 866
- Soifer, B. T., Neugebauer, G., Matthews, K., et al. 2000, *AJ*, 119, 509
- Teng, S. H., Wilson, A. S., Veilleux, S., et al. 2005, *ApJ*, 633, 664
- Teng, S. H., Veilleux, S., Anabuki, N., et al. 2009, *ApJ*, 691, 261
- Teng, S. H., Schawinski, K., Urry, C. M., et al. 2012, *ApJ*, 753, 165
- Thorne, K. S. 1974, *ApJ*, 191, 507
- Tingay, S. J., & Wayth, R. B. 2011, *ApJ*, 141, 174
- U., B., Medling, A., Sanders, D. B., et al. 2013, *ApJ*, 775, 115
- Ueno, S., Koyama, K., Awaki, H., Hayashi, I., & Blanco, P. R. 1996 *PASJ* 48 389
- van Wassenhove, S., Volonteri, M., Mayer, L., et al. 2012, *ApJ*, 748, L7
- Veilleux, S., Kim, D. -C., & Sanders, D. B. 1999a, *ApJ*, 522, 113
- Veilleux, S., Kim, D. -C., Sanders, D. B., Mazzarella, J. M., & Soifer, B. T. 1995, *ApJS*, 98, 171
- Veilleux, S., Sanders, D. B., & Kim, D. -C. 1997, *ApJ*, 484, 92
- Veilleux, S., Sanders, D. B., & Kim, D. -C. 1999b, *ApJ*, 522, 139
- Veilleux, S., Rupke, D. S. N., Kim, D.-C., et al. 2009, *ApJS*, 182, 628
- Videla, L., Lira, P., Andrews, H., et al. 2013, *ApJS*, 204, 23
- Vika, M., Driver, S. P., Cameron, E., Kelvin, L., & Robotham, A. 2012, *MNRAS*, 419, 2264
- Voit, G. M. 1992, *MNRAS*, 258, 841
- Wang, J.-M., Chen, Y.-M., Hu, C., et al. 2009, *ApJ*, 705, L76
- Wang, X. -W., & Zhou, H. -Y. 2012, *ApJ*, 757, 124
- White, R. L., Becker, R. H., Gregg, M. D., et al. 2000, *ApJS*, 126, 133
- White, S. D. M., & Rees, M. J. 1978, *MNRAS*, 183, 341
- Wright, E. L. 2006, *PASP*, 118, 1711
- Wright, E. L., Eisenhardt, P. R. M., Mainzer, A. K., et al. 2010, *AJ*, 140, 1868
- Xia, X. Y., Xue, S. J., Mao, S., et al. 2002, *ApJ*, 564, 196
- Yu, Q., Lu, Y., Mohayaee, R., & Colin, J. 2011, *ApJ*, 738, 92
- Yuan, T. -T., Kewley, L. J., Sanders, D. B. 2010, *ApJ*, 709, 884
- Zhou, S., Wynn-Williams, C. G., & Sanders, D. B. 1993, *ApJ*, 409, 149

TABLE 1
 PROPERTIES OF THE OBSERVED INFRARED LUMINOUS MERGING GALAXIES

Object (1)	z (2)	f_{12} (Jy) (3)	f_{25} (Jy) (4)	f_{60} (Jy) (5)	f_{100} (Jy) (6)	$\log L_{\text{IR}}$ (L_{\odot}) (7)	Optical Class (8)	AGN in the main nucleus ? (9)
IRAS 00091–0738	0.118	<0.07	0.22	2.63	2.52	12.2	HII ^a (cp ^b)	Y ^{1,2,3}
IRAS 00188–0856	0.128	<0.12	0.37	2.59	3.40	12.4	LI ^a (Sy2 ^b)	Y ^{1,2,3,4,5}
IRAS 05024–1941	0.192	0.15	0.14	1.06	1.34	12.5	Sy2 ^{a,b}	Y ^{2,3}
IRAS 05189–2524	0.042	0.73	3.44	13.67	11.36	12.1	Sy2 ^{a,b}	Y ^{2,3,6,7,8,9,10,11,12,13,14,15}
IRAS 08572+3915	0.058	0.32	1.70	7.43	4.59	12.1	LI ^a (Sy2 ^b)	Y ^{1,2,3,4,7,9,12,14,16,17}
IRAS 12127–1412	0.133	<0.13	0.24	1.54	1.13	12.2	LI ^a (HII ^b)	Y ^{1,2,3,4,5}
IRAS 12540+5708 (Mrk 231)	0.042	1.87	8.66	31.99	30.29	12.5	Sy1 ^{a,b}	Y ^{2,3,5,7,9,12,18,19}
IRAS 13335–2612	0.125	<0.13	<0.14	1.40	2.10	12.1	LI ^a (cp ^b)	Y ²
IRAS 13428+5608 (Mrk 273)	0.038	0.24	2.28	21.74	21.38	12.1	Sy2 ^{a,b}	Y ^{2,3,6,7,8,12,13,15,20,21,22,23}
IRAS 13443+0802	0.135	<0.12	<0.11	1.50	1.99	12.2	HII+Sy2 ^a (cp+Sy2 ^b)	N
IRAS 13451+1232 (PKS 1345+12)	0.122	0.14	0.67	1.92	2.06	12.3	Sy2 ^{a,b}	Y ^{2,3,4,5,11,13,15,24}
IRAS 14348–1447	0.083	0.07	0.49	6.87	7.07	12.3	LI ^a (cp ^b)	Y ^{1,2,3,4,5,12}
IRAS 15327+2340 (Arp 220)	0.018	0.48	7.92	103.33	112.40	12.1	LI ^{a,b}	Y ^{2,3,12,15,25}
IRAS 16468+5200	0.150	<0.06	0.10	1.01	1.04	12.1	LI ^a (cp ^b)	Y ^{1,3,14}
IRAS 16474+3430	0.111	<0.13	0.20	2.27	2.88	12.2	HII ^a (cp ^b)	Y ⁴
IRAS 16487+5447	0.104	<0.07	0.20	2.88	3.07	12.2	LI ^a (cp ^b)	Y ^{3,4}
IRAS 17044+6720	0.135	<0.07	0.36	1.28	0.98	12.2	LI ^a (Sy2 ^b)	Y ^{1,3,4,14}
IRAS 21208–0519	0.130	<0.09	<0.15	1.17	1.66	12.0	HII ^a (cp ^b)	Y ²
IRAS 23233+2817	0.114	<0.13	0.28	1.26	2.11	12.1	Sy2 ^{a,b}	Y ⁵
IRAS 23234+0946	0.128	<0.06	0.08	1.56	2.11	12.1	LI ^a (cp ^b)	Y ^{2,3}
IRAS 23327+2913	0.107	<0.06	0.22	2.10	2.81	12.1	LI ^a (Sy2 ^b)	Y ^{1,3}
IRAS 23389+0300	0.145	<0.09	<0.35	1.23	1.17	12.2	Sy2 ^{a,b}	N
IRAS 23498+2423	0.212	<0.10	0.12	1.02	1.45	12.5	Sy2 ^{a,b}	Y ^{2,3,13,14,24}
UGC 5101	0.040	0.25	1.03	11.54	20.23	12.0	LI ^c (Sy2 ^b)	Y ^{2,12,13,14,26,27}
Mrk 463	0.051	0.51	1.58	2.18	1.92	11.8	Sy2 ^{d,e,f}	Y ^{11,12,13,24,28,29}
Mrk 739	0.030	0.16	0.31	1.26	2.41	10.9	Sy1+HII ^g	Y ³⁰
NGC 3393	0.013	0.13	0.75	2.25	3.87	10.4	Sy2 ^h	Y ³¹
NGC 6240	0.024	0.56	3.42	22.68	27.78	11.8	LI ^{b,c}	Y ^{2,12,13,32}
IRAS 20210+1121	0.056	0.29	1.40	3.39	2.68	11.9	Sy2+LI ⁱ	Y ³³

NOTE. — Col.(1): Object name. Col.(2): Redshift. Cols.(3)–(6): f_{12} , f_{25} , f_{60} , and f_{100} are IRAS fluxes at 12 μm , 25 μm , 60 μm , and 100 μm . For the first 23 galaxies, the flux is derived from Kim & Sanders (1998). For the last six galaxies, we use the IRAS Faint Source Catalog. Col.(7): Decimal logarithm of infrared (8–1000 μm) luminosity in units of solar luminosity (L_{\odot}), calculated with $L_{\text{IR}} = 2.1 \times 10^{39} \times D(\text{Mpc})^2 \times (13.48 \times f_{12} + 5.16 \times f_{25} + 2.58 \times f_{60} + f_{100})$ [ergs s⁻¹] (Sanders & Mirabel 1996), where we adopt $H_0 = 71 \text{ km s}^{-1} \text{ Mpc}^{-1}$, $\Omega_M = 0.27$, and $\Omega_{\Lambda} = 0.73$ (Komatsu et al. 2009), to estimate the luminosity distance D (Mpc) from the redshift. Col.(8): Optical spectral classification and references. Sy1, Sy2, LI, HII, and cp mean Seyfert 1, Seyfert 2, LINER, HII-region, and starburst+AGN composite type, respectively. ^a: Veilleux et al. (1999a). ^b: Yuan et al. (2010). ^c: Veilleux et al. (1995). ^d: Shuder & Osterbrock (1981). ^e: Hutchings & Neff (1989). ^f: Sanders et al. (1988). ^g: Koss et al. (2011). ^h: Diaz et al. (1988). ⁱ: Perez et al. (1990). Col.(9): The presence of AGN signatures in the brightest main nucleus (Y = yes, N = no), and several selected representative references. ¹: Imanishi et al. (2007). ²: Veilleux et al. (2009). ³: Nardini et al. (2010). ⁴: Imanishi et al. (2006a). ⁵: Imanishi et al. (2010b). ⁶: Veilleux et al. (1999b). ⁷: Imanishi & Dudley (2000). ⁸: Risaliti et al. (2000). ⁹: Soifer et al. (2000). ¹⁰: Severgnini et al. (2001). ¹¹: Imanishi & Terashima (2004). ¹²: Armus et al. (2007). ¹³: Farrah et al. (2007). ¹⁴: Imanishi et al. (2008). ¹⁵: Teng et al. (2009). ¹⁶: Dudley & Wynn-Williams (1997). ¹⁷: Imanishi et al. (2011b). ¹⁸: Maloney & Reynolds (2000). ¹⁹: Braito et al. (2004). ²⁰: Xia et al. (2002). ²¹: Balestra et al. (2005). ²²: Iwasawa et al. (2011a). ²³: U et al. (2013). ²⁴: Veilleux et al. (1997). ²⁵: Downes & Eckart (2007). ²⁶: Imanishi et al. (2001). ²⁷: Imanishi et al. (2003). ²⁸: Ueno et al. (1996). ²⁹: Bianchi et al. (2008). ³⁰: Koss et al. (2011). ³¹: Fabbiano et al. (2011). ³²: Komossa et al. (2003). ³³: Piconcelli et al. (2010).

TABLE 2
OBSERVATION LOG

Object	Band	Date (UT)	Exposure (min)	Standard Star Name	Star mag	LGS-AO or NGS-AO guide star Name USNO	R-band mag	separation (arcsec)
(1)	(2)	(3)	(4)	(5)	(6)	(7)	(8)	(9)
IRAS 00091–0738	K	2011 August 23	11.3	FS2	10.5	0826-0002500	17	57
	L'	2011 August 22, 23	27	HD 1160	7.1	0826-0002500	17	57
IRAS 00188–0856	K	2011 August 23	11.7	FS2	10.5	0813-0003721	16	24
	L'	2011 August 22	9	HD1160	7.1	0813-0003721	16	24
IRAS 05024–1941	K	2012 October 16	9	FS13	10.1	0703-0054437	15	10
	L'	2012 October 16	27	HD22686	7.2	0703-0054437	15	10
IRAS 05189–2524	K	2012 October 16	9	FS13	10.1	nucleus	11	0
	L'	2012 October 16	9	HD22686	7.2	nucleus	11	0
IRAS 08572+3915	K	2012 April 15	4.5	FS125	10.4	1290-0192776	14	58
	L'	2012 April 15	13.5	HD84800	7.5	1290-0192776	14	58
IRAS 12127–1412	K	2012 May 20	9	FS132	11.8	0755-0260793	13	20
	L'	2012 May 20	9	HD106965	7.3	0755-0260793	13	20
Mrk 231	K	2013 May 8	15.6	FS133	11.9	nucleus ^a	9	0
	L'	2013 May 8	13.7	HD129653	6.9	nucleus ^a	9	0
IRAS 13335–2612	K	2012 May 20	9	S791-C	11.2	0635-0309957	14	43
	L'	2012 May 20	18	HD106965	7.3	0635-0309957	14	43
Mrk 273	K	2013 May 8	9	FS133	11.9	1458-0231011 ^a	16	34
	L'	2013 May 8	22.5	HD129653	6.9	1458-0231011 ^a	16	34
IRAS 13443+0802	K	2012 May 20	9	S791-C	11.2	0977-0294304	16	57
	L'	2012 May 20	18	HD106965	7.3	0977-0294304	16	57
PKS 1345+12	K	2012 March 23	4	P272D	11.2	western nucleus	12	0
	L'	2012 March 23	9	HD136754	7.2	western nucleus	12	0
IRAS 14348–1447	K	2012 April 15	9	FS132	11.8	0749-0288838	15	27
	L'	2012 April 15	13.5	HD106965	7.3	0749-0288838	15	27
Arp 220	K	2012 April 15	9	P272D	11.2	nucleus	8	0
	L'	2012 April 15	13.5	HD136754	7.2	nucleus	8	0
IRAS 16468+5200	K	2011 August 23	12	p138-c	11.1	1419-0298775	18	37
	L'	2011 August 23	13.5	HD162208	7.1	1419-0298775	18	37
IRAS 16474+3430	K	2011 July 30	8	FS 139	12.1	1244-0244739	15	17
	L'	2012 May 20	18	HD136754	7.2	1244-0244739	15	17
IRAS 16487+5447	K	2011 August 23	11.3	p138-c	11.1	1447-0253801	13	54
	L'	2011 August 23	13.5	HD162208	7.1	1447-0253801	13	54
IRAS 17044+6720	K	2012 April 15	9	P272D	11.2	1572-0201777	14	62
	L'	2012 April 15	4.5	HD136754	7.2	1572-0201777	14	62
IRAS 21208–0519	K	2011 August 23	15	S813D	11.1	0848-0617074	15	17
	L'	2011 August 23	22.5	GL811.1	6.7	0848-0617074	15	17
IRAS 23233+2817	K	2012 October 16	9	FS155	9.4	1185-0599614	14	63
	L'	2012 October 16	13.5	HD203856	6.9	1185-0599614	14	63
IRAS 23234+0946	K	2011 August 22	11.3	FS154	11.1	1000-0612015	18	61
	L'	2011 August 22	9	HD1160	7.1	1000-0612015	18	61
IRAS 23327+2913	K	2011 August 23	11.3	FS155	9.4	1194-0587875	18	36
	L'	2012 October 16	18	HD203856	6.9	1194-0587875	18	36
IRAS 23389+0300	K	2011 August 22	11.3	FS154	11.1	0932-0712575	16	52
	L'	2011 August 22	13.5	HD1160	7.1	0932-0712575	16	52
IRAS 23498+2423	K	2012 October 16	9	FS155	9.4	north-western nucleus	17	0
	L'	2012 October 16	9	HD203856	6.9	north-western nucleus	17	0
UGC 5101	K	2012 April 15	3.75	FS125	10.4	1513-0178261	15	15
	L'	2012 April 15	9	HD84800	7.5	1513-0178261	15	15
Mrk 463	K	2012 March 23	9	P272D	11.2	1083-0240150	17	65
	L'	2012 March 23	9	HD136754	7.2	1083-0240150	17	65
Mrk 739	K	2012 April 15	9	FS125	10.4	1116-0211017	17	31
	L'	2012 April 15	13.5	HD84800	7.5	1116-0211017	17	31
NGC 3393	K	2012 May 20	9	FS132	11.8	0648-0254969	16	55
	L'	2012 May 20	9	HD106965	7.3	0648-0254969	16	55
NGC 6240	K	2011 June 20	48	FS137	11.8	0924-0386013 ^a	12	37
	L'	2011 June 20	5	HD129655	6.7	0924-0386013 ^a	12	37
IRAS 20210+1121	K	2011 June 20	7.5	FS149	10.1	1015-0589702 ^a	13	47
	L'	2011 June 20	6.3	HD201941	6.6	1015-0589702 ^a	13	47

NOTE. — Col.(1): Object name. Col.(2): Observed band. *K*- or *L'*-band. Col.(3): Observing date in UT. Col.(4): Net on-source exposure time in min. Col.(5): Standard star's name. Col.(6): Standard star's magnitude in the *K*- or *L'*-band. Col.(7): Guide star name (USNO number) used for the LGS-AO tip-tilt correction or NGS-AO correction. Col.(8): Guide star's optical *R*-band magnitude. Col.(9): Separation between the target object and guide star in arcsec.

^aNGS-AO guide star

TABLE 3
NUCLEAR PHOTOMETRY AND ESTIMATED AGN COMPONENT

Object	$K(0''.5)$ (mag)	$L'(0''.5)$ (mag)	$K - L'(0''.5)$ (mag)	AGN (%)	L_{AGN} (10^{44} ergs s^{-1})	WISE($3.4\mu\text{m}$) (mag)
(1)	(2)	(3)	(4)	(5)	(6)	(7)
IRAS 00091–0738 S	15.7	14.7	1.0±0.2	49	0.045	13.7 ^A
IRAS 00091–0738 N	16.5	>15.3	<1.2	<64	<0.034	13.7 ^A
IRAS 00188–0856	13.9	12.7	1.2±0.2	63	0.44	12.3
IRAS 05024–1941 E	15.1	13.9	1.2±0.2	63	0.35	13.3 ^A
IRAS 05024–1941 W	15.8	>15.3	<0.5	0	0	13.3 ^A
IRAS 05189–2524	10.9	8.6	2.3±0.2	100	2.9	8.7
IRAS 08572+3915 NW	13.8	9.3 ^B	4.5±0.2	100	3.0	10.3
IRAS 08572+3915 SE	16.5	>14.8 ^B	<1.7	<90	<0.017	...
IRAS 12127–1412 NE	13.5	10.7	2.8±0.2	100	4.8	10.9
IRAS 12127–1412 SW	18.3	>15.2	<3.1	<100	<0.076	...
Mrk 231	9.2	7.2 ^C	2.0±0.2	100	10	7.4
IRAS 13335–2612 N	15.6	14.8	0.8±0.2	32	0.030	13.0 ^A
IRAS 13335–2612 S	15.3	14.2	1.1±0.2	57	0.094	13.0 ^A
IRAS 13335–2612 SE	16.0	>15.4	<0.6	<12	<0.0066	13.0 ^A
Mrk 273 SW	13.6	11.3 ^D	2.3±0.2	100	0.19	10.4 ^A
Mrk 273 NE	13.1	11.5 ^D	1.6±0.2	85	0.14	10.4 ^A
IRAS 13443+0802 NE	14.6	14.1	0.5±0.2	0	0	12.7
IRAS 13443+0802 E	16.1	14.6	1.5±0.2	80	0.11	13.8
IRAS 13443+0802 SW	16.8	>15.3	<1.5	<81	<0.058	14.8
PKS 1345+12 W	14.4	11.4	3.0±0.2	100	2.1	11.4 ^A
PKS 1345+12 E	15.6	>14.6	<1.0	<50	<0.054	11.4 ^A
IRAS 14348–1447 SW	14.3	13.4	0.9±0.2	41	0.059	12.1 ^A
IRAS 14348–1447 NE	15.0	13.7	1.3±0.2	70	0.076	12.1 ^A
Arp 220 W	13.0	11.7	1.3±0.2	70	0.021	10.1 ^A
Arp 220 E	13.2	12.1	1.1±0.2	57	0.012	10.1 ^A
IRAS 16468+5200 E	16.5	15.0	1.5±0.2	80	0.094	14.4 ^A
IRAS 16468+5200 W	16.7	>15.6	<1.1	<57	<0.039	14.4 ^A
IRAS 16474+3430 S	14.6	13.6	1.0±0.2	49	0.11	12.3 ^A
IRAS 16474+3430 M ^E	14.8	13.7	1.1±0.2	57	0.12	12.3 ^A
IRAS 16487+5447 SW	15.7	14.6	1.1±0.2	57	0.044	13.1 ^A
IRAS 16487+5447 NE	16.0	>15.2	<0.8	<33	<0.015	13.1 ^A
IRAS 17044+6720	14.5	11.9	2.6±0.2	100	1.6	12.0
IRAS 21208–0519 NE	15.1	14.5	0.6±0.2	12	0.016	13.2
IRAS 21208–0519 SW	16.1	>16.0	<0.1	0	0	...
IRAS 23233+2817 N	14.6	12.7	1.9±0.2	97	0.52	12.5 ^A
IRAS 23233+2817 S	16.3	>15.0	<1.3	<70	<0.046	12.5 ^A
IRAS 23234+0946 NW	15.2	13.7	1.5±0.2	80	0.22	13.4 ^A
IRAS 23234+0946 SE	16.7	>14.3	<2.4	<100	<0.16	13.4 ^A
IRAS 23327+2913 S	14.5	13.2	1.3±0.2	70	0.21	12.8
IRAS 23327+2913 N	15.7	>14.9	<0.8	<33	<0.020	13.8
IRAS 23389+0300 N	15.0	14.0	1.0±0.2	49	0.13	13.7 ^A
IRAS 23389+0300 S	17.1	>15.1	<2.0	<100	<0.10	13.7 ^A
IRAS 23498+2423 NW	13.7	11.4	2.3±0.2	100	7.0	11.5 ^A
IRAS 23498+2423 SE	17.4	>15.4	<2.0	<100	<0.18	11.5 ^A
UGC 5101	12.0	9.5	2.5±0.2	100	1.1	10.0
Mrk 463 E	10.9	8.3	2.6±0.2	100	5.5	8.5 ^A
Mrk 463 W	14.1	13.3	0.8±0.2	32	0.017	8.5 ^A
Mrk 739 E	12.2	10.2	2.0±0.2	100	0.33	9.9
Mrk 739 W	14.2	13.8	0.4±0.2	0	0	...
NGC 3393	13.0	11.9	1.1±0.2	57	0.0072	10.0
NGC 6240 S ^F	11.8	10.5 ^G	1.3±0.2	70	0.11	9.3 ^A
NGC 6240 N ^F	13.0	11.9 ^G	1.1±0.2	57	0.025	9.3 ^A
IRAS 20210+1121 S	13.5	11.0	2.5±0.2	100	0.57	11.2
IRAS 20210+1121 N	14.6	13.9	0.7±0.2	22	0.0087	...

NOTE. — Col.(1): Object name. Col.(2): K -band ($2.2\mu\text{m}$) magnitude within the central $\sim 0''.5$ -radius aperture (10 pixels for $52.77\text{ mas pixel}^{-1}$ data). For Mrk 231, the $0''.5$ aperture is set from 25 pixels \times $20.57\text{ mas pixel}^{-1}$. The possible uncertainty for spatially unresolved compact emission is taken as $<0.3\text{ mag}$ (see §4.2). Col.(3): L' -band ($3.8\mu\text{m}$) magnitude within the central $\sim 0''.5$ -radius aperture (25 pixels for $20.57\text{ mas pixel}^{-1}$ data). The possible uncertainty for spatially unresolved compact emission is taken as $<0.2\text{ mag}$ (see §4.2). For undetected L' -band nuclei, the upper limits are derived at the K -band peak position based on 3σ of sky fluctuation. Col.(4): $K - L'$ color magnitude within the central $\sim 0''.5$ -radius aperture. The possible uncertainty for spatially unresolved compact emission is regarded as $<0.2\text{ mag}$ (see §4.2). Col.(5): AGN fraction in the L' -band in %. Col.(6): AGN luminosity in $10^{44}\text{ ergs s}^{-1}$ from AGN-origin νF_ν value at L' after removing the starburst contribution. The possible uncertainty is $<0.2\text{ mag}$ in the sense that the AGN luminosity may be underestimated. Col.(7): WISE $3.4\mu\text{m}$ photometric magnitude with $6''.1$ angular resolution, for comparison (Wright et al. 2010).

^A More than one nucleus combined, due to low-spatial-resolution data.

^B Zhou et al. (1993) estimated 10.0 mag and $>15.0\text{ mag}$ at $3.4\mu\text{m}$ using a $2''.5$ aperture for the NW and SE nuclei, respectively. For the NW nucleus, our L' -band ($3.8\mu\text{m}$) magnitude, measured with a smaller aperture, is $\sim 0.7\text{ mag}$ brighter, which can naturally be explained by a very red, steeply rising continuum flux from $3.4\mu\text{m}$ to $3.8\mu\text{m}$ (Imanishi et al. 2008).

^C Zhou et al. (1993) estimated 7.5 mag at $3.4\mu\text{m}$ using a $2''.5$ aperture. Our measurement at L' with a

TABLE 4
COMPARISON OF OUR K -BAND ($2.2 \mu\text{m}$) PHOTOMETRY WITH $2.2 \mu\text{m}$
PHOTOMETRY BY SCOVILLE ET AL. (2000)

Object	2.2 μm mag Scoville et al. (2000)	K -mag our data	Difference
(1)	(2)	(3)	(4)
IRAS 05189–2524	10.33	10.9	0.57
IRAS 08572+3915 N	13.53	13.8	0.27
IRAS 08572+3915 S	15.76	16.5	0.74
Mrk 273 S	13.29	13.6	0.31
Mrk 273 N	12.91	13.1	0.19
PKS 1345+12 W	13.96	14.4	0.44
PKS 1345+12 E	15.31	15.6	0.29
IRAS 14348–1447 S	14.19	14.3	0.11
IRAS 14348–1447 N	14.92	15.0	0.08
Arp 220 W	12.79	13.0	0.21
Arp 220 E	13.13	13.2	0.07
UGC 5101	11.77	12.0	0.23
NGC 6240 S	11.36	11.8	0.44
NGC 6240 N	12.72	13.0	0.28

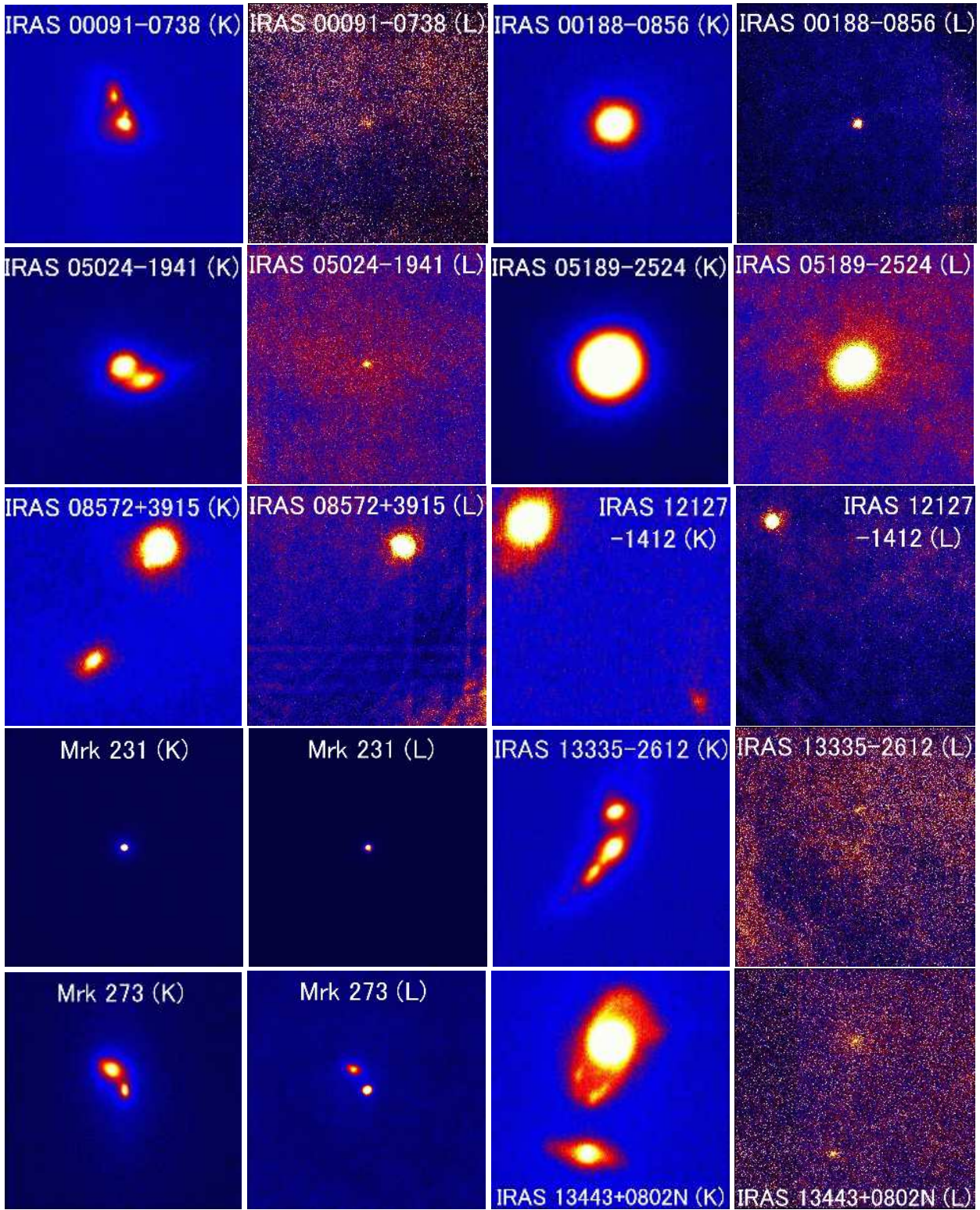
NOTE. — Col.(1): Object name. Col.(2): Nuclear $1''$ -diameter magnitude at $2.2 \mu\text{m}$ derived by Scoville et al. (2000). Col.(3): Nuclear $0''.5$ -radius ($1''.0$ diameter) K -band ($2.2 \mu\text{m}$) magnitude based on our data. Col.(4): Difference in the photometry between Scoville et al. (2000) and our data. For all sources, our data tend to show slightly fainter photometric magnitudes than computed by Scoville et al. (2000) due to the smaller aperture size and the signal spread into the seeing-sized halo outside the AO core.

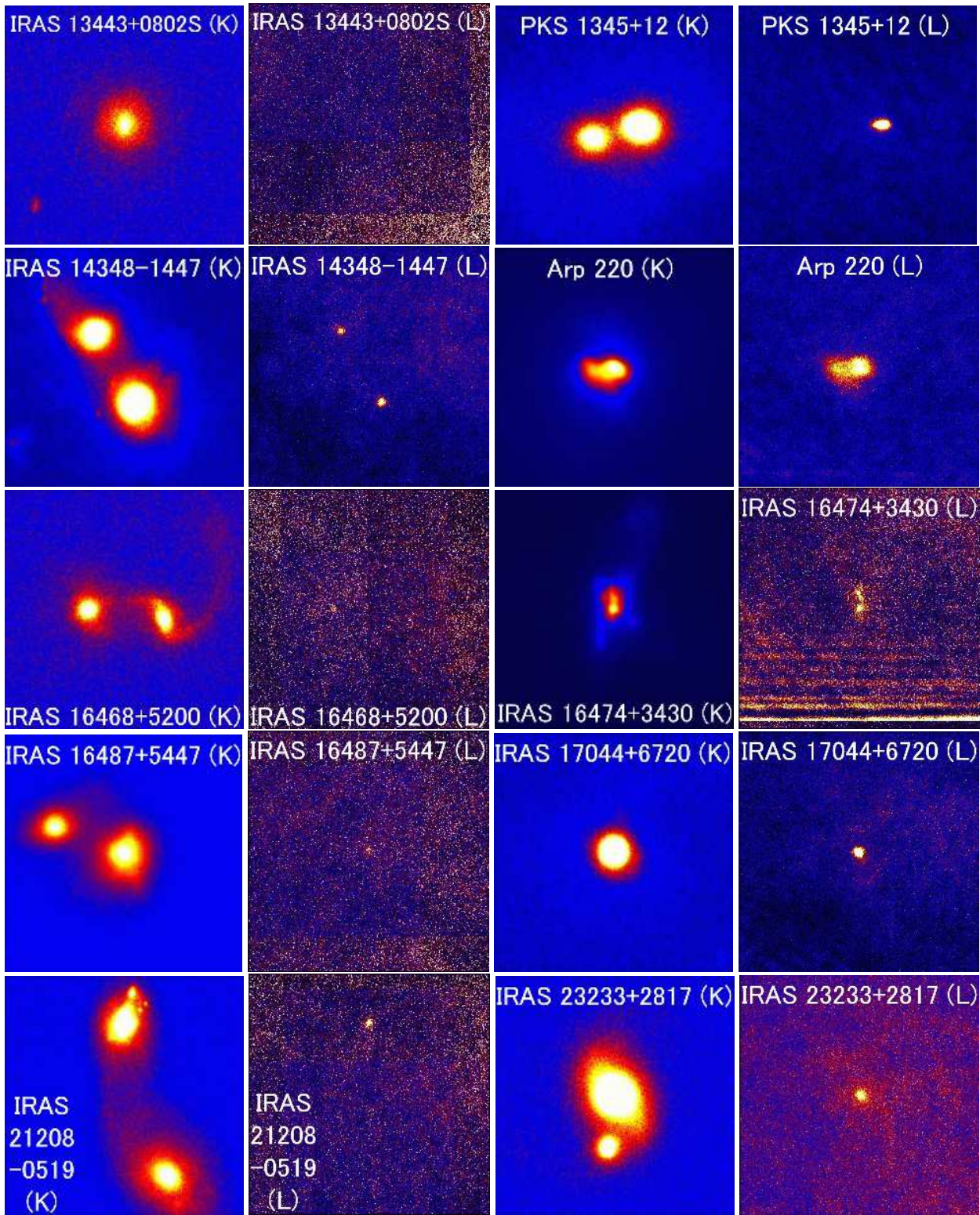
TABLE 5
LUMINOSITY RATIO AND NUCLEAR SEPARATION IN SEEING-BASED MULTIPLE NUCLEI (U)LIRGS

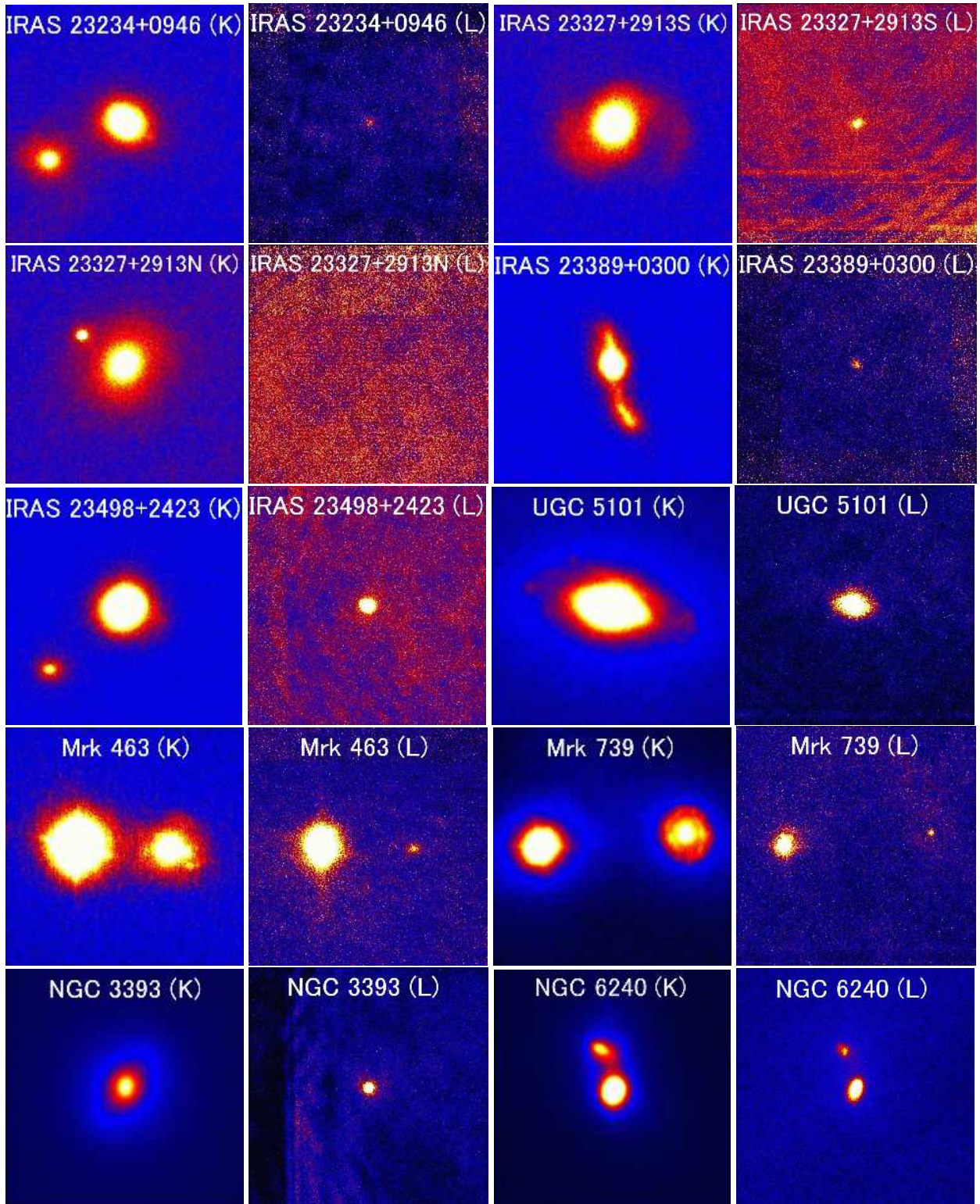
Object	K (stellar) ratio	L' ratio	L' (AGN) ratio	Separation (arcsec)	Separation (kpc)
(1)	(2)	(3)	(4)	(5)	(6)
IRAS 00091–0738 N, S	1.35 (15.34, 15.67)	<0.58	<0.76	1.2	2.6
IRAS 08572+3915 NW, SE	6.37 (13.66, 15.67)	>158	>176	5.5	6.1
IRAS 12127–1412 NE, SW	75.9 (13.63, 18.33)	>63	>63	10.4	24.2
IRAS 13335–2612 S, N	1.20 (15.20, 15.40) ^A	1.7	3.1	1.6	3.5
IRAS 13443+0802 NE, E	4.02 (14.52, 16.03)	1.6	0	4.8	11.3
IRAS 13443+0802 E, SW	1.80 (16.03, 16.67)	>1.9	>1.8	13.4	31.7
PKS 1345+12 W, E	2.31 (14.54, 15.45) ^A	>19	>38	2.0	4.4
IRAS 14348–1447 SW, NE	1.64 (13.98, 14.52) ^A	1.3	0.78	3.4	5.2
IRAS 16468+5200 E, W	1.19 (16.64, 16.83)	>1.7	>2.4	3.2	8.3
IRAS 16487+5447 SW, NE	1.53 (14.89, 15.35)	>1.7	>2.9	3.1	5.9
IRAS 21208–0519 NE, SW	2.15 (15.16, 15.99)	>3.9	∞	6.6	15.2
IRAS 23234+0946 NW, SE	3.70 (15.32, 16.74) ^A	>1.7	>1.3	3.5	8.0
IRAS 23327+2913 S, N	2.54 (14.29, 15.30)	>4.7	>10	12.5	24.1
IRAS 23389+0300 N, S	6.49 (15.08, 17.11)	>2.7	>1.3	2.3	5.7
IRAS 23498+2423 NW, SE	32.8 (14.08, 17.87)	>39	>38	4.1	13.9
Mrk 463 E, W	1.74 (10.49, 11.09)	100	324	3.9	3.8
Mrk 739 E, W	3.53 (11.37, 12.74)	28	∞	6.1	3.6
IRAS 20210+1121 S, N	2.25 (12.76, 13.64)	15	66	12.3	13.2

NOTE. — Col.(1): Object name. Col.(2): K -band flux ratio, measured with the same aperture size between two nuclei, as an approximation of stellar emission luminosity ratio. K -band photometric values in individual nuclei are shown in parentheses; the first value is for the nucleus shown first in column 1. The 4-kpc aperture K -band photometry by Kim et al. (2002) is basically adopted, but for the last three sources (Mrk 463, Mrk 739, and IRAS 20210+1121), photometry from the 2MASS point source catalog ($4''$ aperture) is employed. Col.(3): Nuclear L' -band ($3.8 \mu\text{m}$) luminosity ratio based on our photometry (Table 3, column 3). Col.(4): Nuclear AGN-origin L' -band ($3.8 \mu\text{m}$) luminosity ratio after the subtraction of stellar emission component (Table 3, column 6). In Cols. (2)–(4), the luminosity at the nucleus listed first in column 1 is divided by that listed second in column 1. Col.(5): Apparent nuclear separation in arcsec calculated from our Subaru LGS/NGS-AO K -band images. Col.(6): Apparent nuclear separation in kpc calculated using $H_0 = 71 \text{ km s}^{-1} \text{ Mpc}^{-1}$, $\Omega_M = 0.27$, and $\Omega_\Lambda = 0.73$ (Komatsu et al. 2009).

^ABased on the velocity dispersion obtained through near-infrared spectroscopy, SMBH mass ratios are computed to be 2.45, 1.72, 0.61, and 3.29 for IRAS 13335–2612 (S, N), PKS 1345+12 (W, E), IRAS 14348–1447 (SW, NE), and IRAS 23234+0946 (NW, SE), respectively (Dasyra et al. 2006a,b).







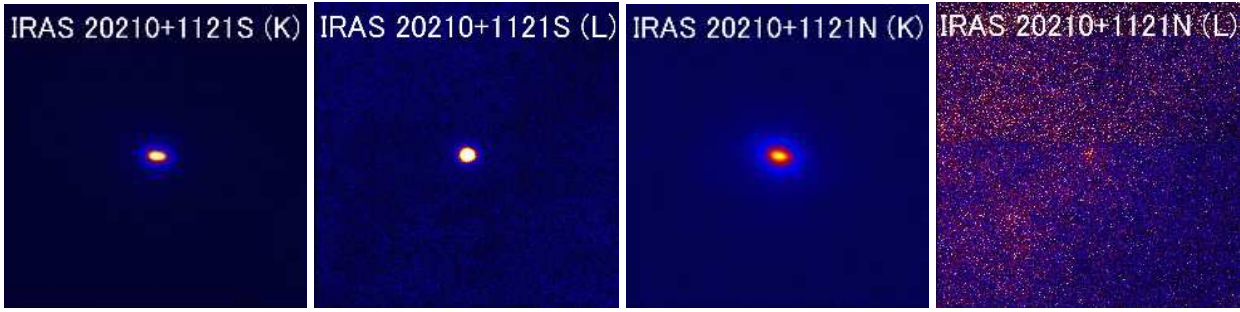


FIG. 1.— Our Subaru AO K - ($2.2 \mu\text{m}$) and L' -band ($3.8 \mu\text{m}$) images of observed (U)LIRG nuclei. The field of view (FOV) is $10'' \times 10''$. North is up, and east is to the left. For IRAS 13443+0802, 23327+2913, and 20210+1121, two separate images are shown because the largest separations of multiple nuclei are $>10''$ (Kim et al. 2002; Piconcelli et al. 2010).

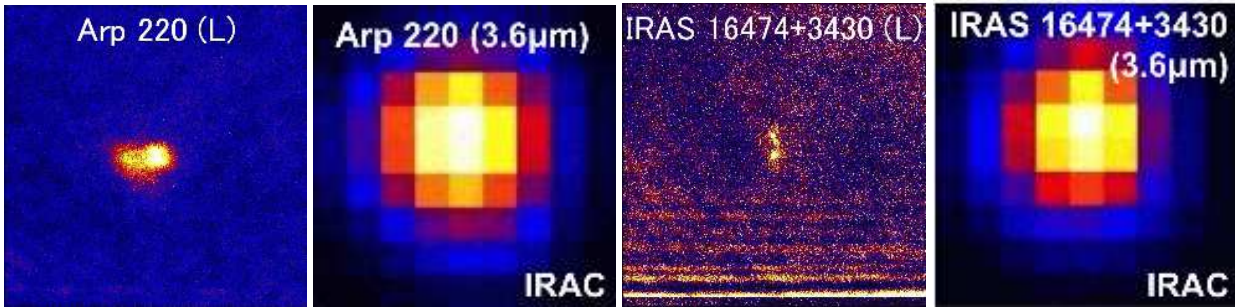


FIG. 2.— Comparison of our Subaru AO L' -band ($3.8 \mu\text{m}$) images with Spitzer IRAC $3.6 \mu\text{m}$ images of two ULIRGs (Arp 220 and IRAS 16474+3430). The FOV is $10'' \times 10''$. North is up, and east is to the left.

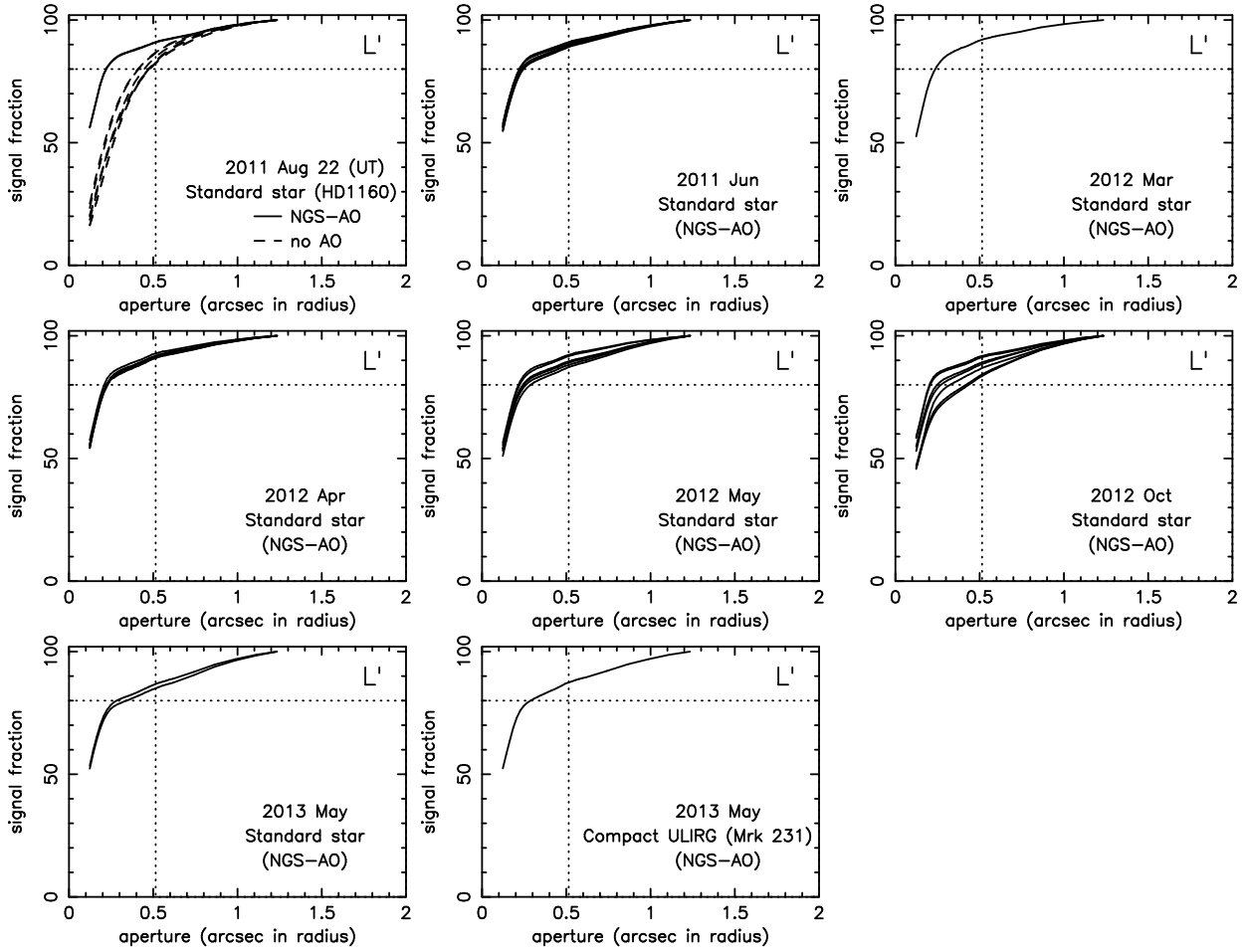


FIG. 3.— The growth of the curve of the encircled signal in the L' -band for standard stars observed with NGS-AO on various nights (Table 2) using the standard stars themselves as AO guide stars. The growth of the signal of a ULIRG dominated by spatially unresolved compact emission (Mrk 231), observed with NGS-AO, is also plotted. For the upper left plot, the growth of the curves of a standard star (HD 1160) observed with NGS-AO (two data sets) and without AO (seven data sets) on the same night (2011 August 22 UT) are shown and compared. NGS-AO data (solid lines) show a higher central concentration of signals than non-AO data (dashed lines), demonstrating the power of Subaru AO for improved photometry of spatially unresolved compact sources using a small aperture. The horizontal and vertical dotted lines indicate an 80% signal fraction and employed $\sim 0''.5$ -radius aperture size, respectively. It is seen that the $\sim 0''.5$ -radius aperture ($25 \text{ pixels} \times 20.57 \text{ mas pixel}^{-1}$) consistently contains 83–93% of spatially unresolved compact source signals in the Subaru L' -band NGS-AO images.

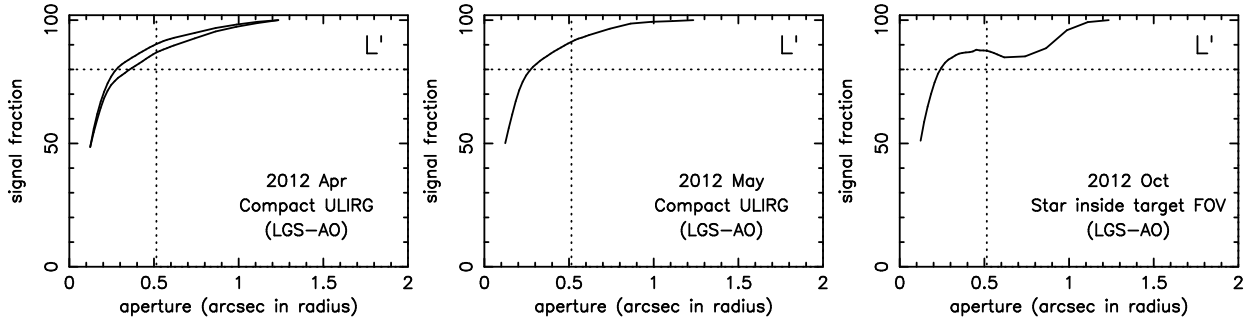


FIG. 4.— The growth of the curve of the encircled signal in the L' -band observed with LGS-AO. (*Left*): Compact merging nuclei with no discernible extended emission component (Mrk 739 eastern nucleus and IRAS 08572+3915 north-western nucleus), observed in 2012 April. In the L' -band images of merging galaxies, it is harder to find bright stars with high detection significance inside frames than in the K -band because of the smaller field of view and larger background noise. For these reasons, compact merging nuclei are used to estimate the signal growth of the curve for LGS-AO at L' . As these merging nuclei could contain spatially extended host galaxy emission components, the signal fraction at each aperture size is a lower limit on the spatially unresolved emission components. (*Middle*): Compact merging nuclei observed in 2012 May (IRAS 12127–1412 north-eastern nucleus). (*Right*): A bright star inside the field of view of IRAS 05024–1941 (USNO 0703-0054437) observed in 2012 October. This star is located at the edge of the L' -band image, where a significant noise pattern is recognizable. The growth of the curve may be affected by this noise. The horizontal and vertical dotted lines indicate the 80% signal fraction and the $\sim 0''.5$ radius aperture size, respectively. In all plots, 85–93% of the signals from spatially unresolved compact sources are recovered using the $\sim 0''.5$ -radius aperture ($25 \text{ pixels} \times 20.57 \text{ mas pixel}^{-1}$) in the Subaru L' -band LGS-AO images. This signal fraction is comparable to that of Subaru L' -band NGS-AO images (Figure 3).

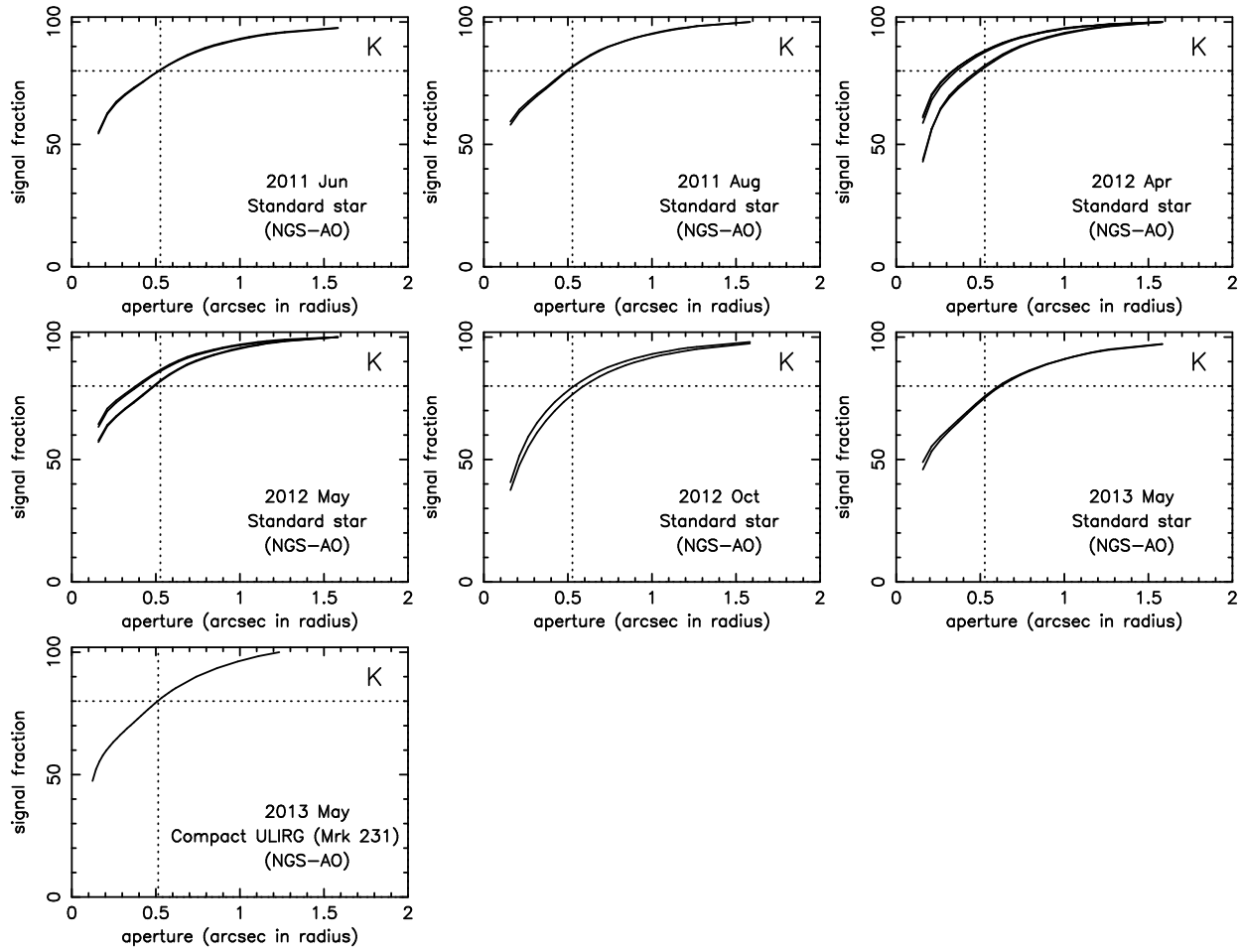


FIG. 5.— The growth of the curve of the encircled signal in the K -band for standard stars observed with NGS-AO during various observation nights (Table 2) using the standard stars themselves as AO guide stars. A plot of a ULIRG dominated by spatially unresolved compact emission (Mrk 231), observed with NGS-AO, is also shown. The horizontal and vertical dotted lines indicate the 80% signal fraction and employed $\sim 0''.5$ radius aperture size, respectively. In all plots, 75–90% of signals from spatially unresolved compact source emission are recovered using a $\sim 0''.5$ -radius aperture ($10 \text{ pixels} \times 52.77 \text{ mas pixel}^{-1}$) for Subaru K -band NGS-AO data. For Mrk 231, the $\sim 0''.5$ radius aperture is set from $25 \text{ pixels} \times 20.57 \text{ mas pixel}^{-1}$ (see § 3).

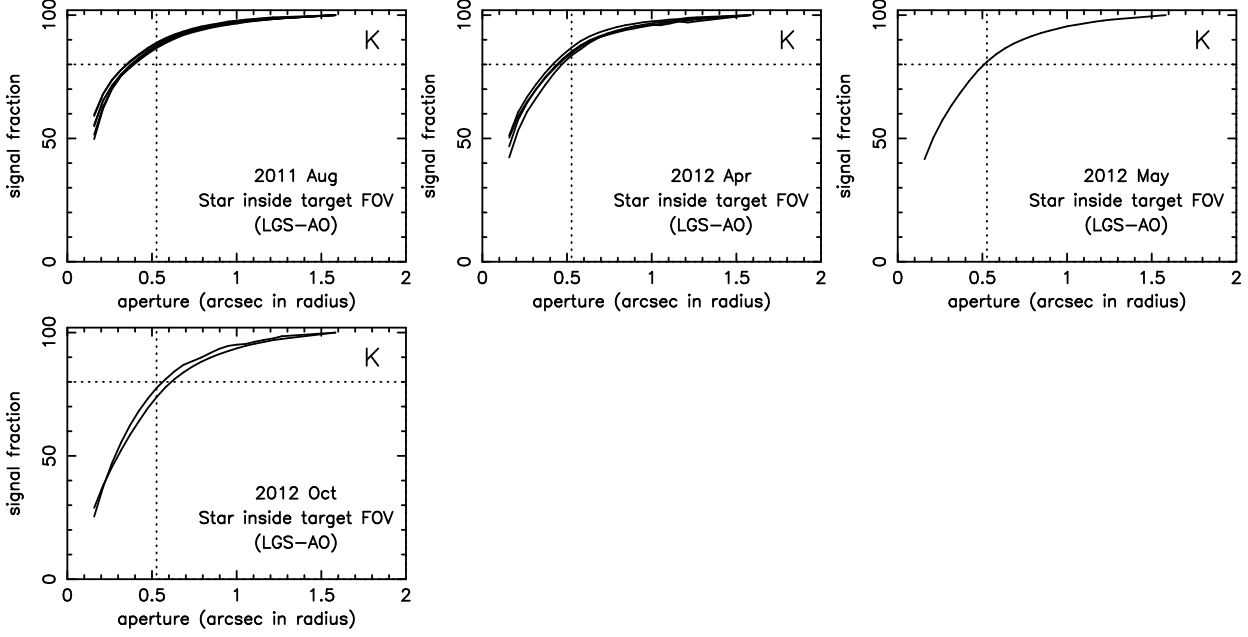


FIG. 6.— The growth of the curve of the encircled signal in the K -band, estimated using bright stars inside the field of view of the target (U)LIRGs, observed with LGS-AO on various nights. (*Upper Left*): Three stars in the IRAS 00188–0856 LGS-AO image (USNO 0813-0003716, 0813-0003719, 0813-0003721) and three stars in the IRAS 21208–0519 LGS-AO image (USNO 0848-0617068, 0848-0617074, 0848-0617085), taken in 2011 August are used. (*Upper Middle*): A bright star in the IRAS 14388–1447 LGS-AO image (USNO 0749-0288838), a star in the IRAS 17044+6720 LGS-AO image (USNO 1572-0201749), and two stars in the Mrk 739 LGS-AO image (USNO 1116-0211017, 1116-0211021) obtained in 2012 April are used. (*Upper Right*): A bright star in the IRAS 12127–1412 LGS-AO image (USNO 0755-0260793), taken in 2012 May, is used. (*Lower Left*): A bright star in the IRAS 05024–1941 LGS-AO image (USNO 0703-0054437) and a bright star $\sim 8''$ west of IRAS 23498+2423 (seen in the K -band image of Kim et al. (2002)) taken in 2012 October are used. The horizontal and vertical dotted lines indicate the 80% signal fraction and $\sim 0''.5$ -radius aperture size, respectively. In all plots, the chosen $\sim 0''.5$ radius aperture recovered 75–90% of the spatially unresolved compact source signals in the Subaru K -band LGS-AO images.

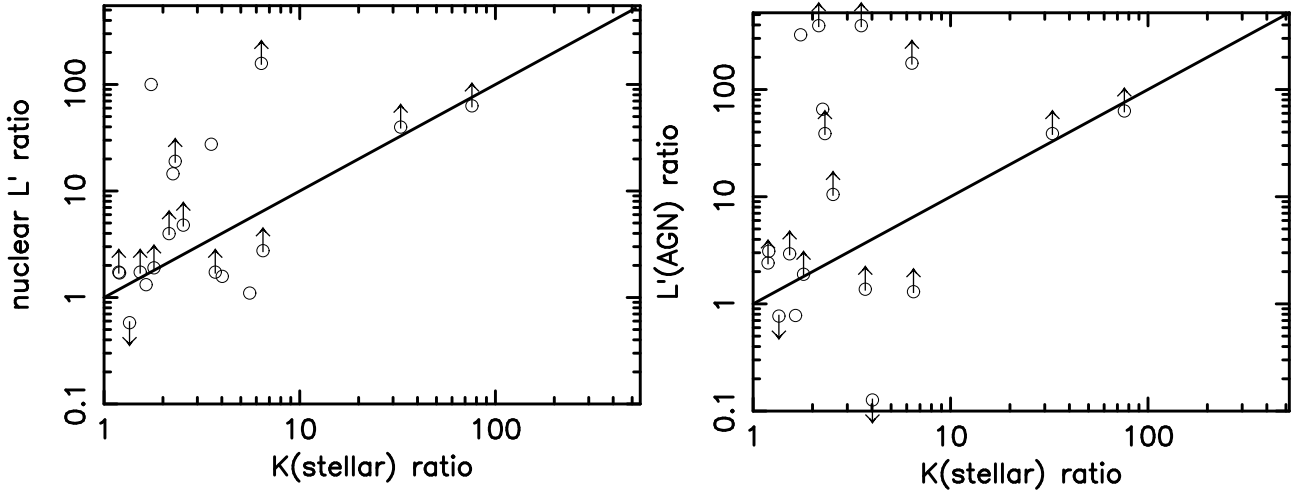


FIG. 7.— (*Left*): Luminosity ratio among multiple nuclei for (U)LIRGs listed in Table 5. The abscissa is the K -band photometry, including host galaxy emission. The ordinate is the nuclear L' -band ($\sim 0''.5$ -radius aperture) photometry (Table 3, column 3). The abscissa is taken as the stellar luminosity ratio, which is converted to the SMBH mass ratio. If AGN-origin L' -band luminosity excess compared with stellar emission is different for multiple nuclei, then the source will deviate from the solid line. (*Right*): The ordinate is the AGN-origin L' -band luminosity ratio after subtracting stellar emission (Table 3, column 6). In the ordinate of both plots, the L' -band luminosity at the brighter nucleus in the K -band stellar emission is divided by that at the K -band fainter nucleus. Sources appearing around the upper-left (lower-right) of the solid line suggest that larger-mass SMBHs show higher (lower) mass accretion rates when normalized to SMBH mass than do smaller-mass SMBHs. The upper (down) arrows in the ordinate indicate sources whose L' -band emission was not detected ($< 3\sigma$) at the K -band fainter (brighter) nuclei.

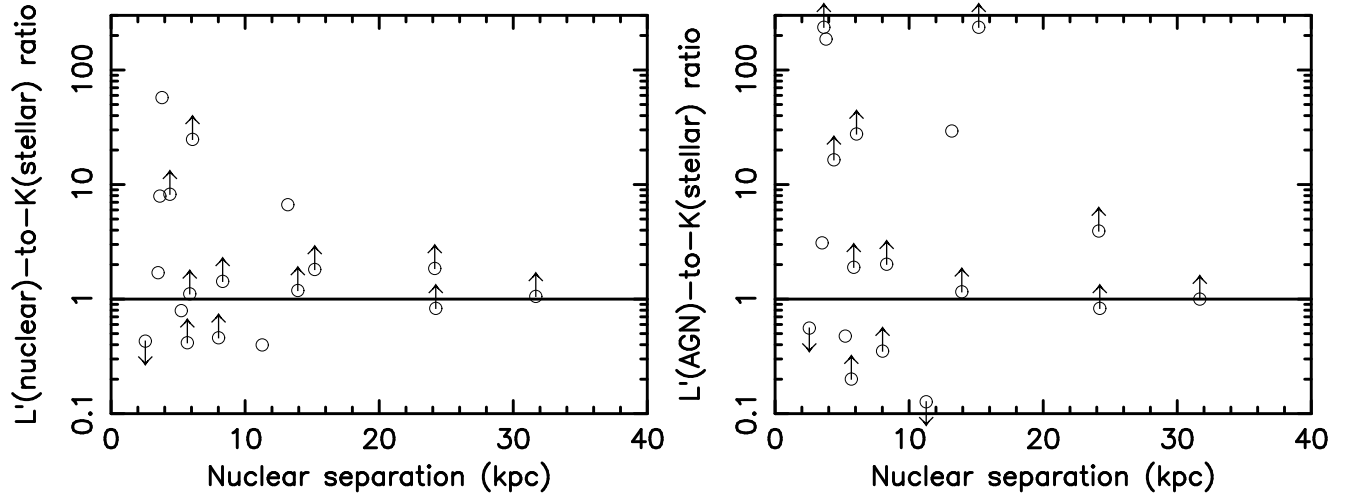


FIG. 8.— (*Left*): The abscissa is apparent nuclear separation in kpc for (U)LIRGs in Table 5. The ordinate is the comparison of the nuclear L' -band to galaxy-wide K -band stellar luminosity ratio between two nuclei. (*Right*): Same as the left panel, but the ordinate is the comparison of the AGN-origin L' -band to K -band stellar luminosity ratio between two nuclei. In both plots, the ratio at the nucleus with brighter K -band stellar emission is divided by that at the nucleus with fainter K -band stellar emission. Since the K -band stellar luminosity is taken to be proportional to the SMBH mass, the ordinate is proportional to the Eddington ratio (= mass accretion rate per SMBH mass). Sources above the solid horizontal lines mean that the Eddington ratios are higher at the K -band brighter nuclei (= nuclei with larger-mass SMBHs). The upper (down) arrows in the ordinate indicate sources whose L' -band emission was not detected ($<3\sigma$) at the K -band fainter (brighter) nuclei.